Submitted version of the paper published as

Kujawa, M., Smakosz, Ł., Paczos, P., Jan, F., Winkelmann, K., Konopińska-Zmysłowska, V. and Eremeyev, V.A., 2026. An analytical, finite element and experimental study of single-lap joints bonded with epoxy adhesive. International Journal of Engineering Science, 226, 104555
doi 10.1016/j.ijengsci.2026.104555
https://www.sciencedirect.com/science/article/pii/S0020722526000935.

Highlights

An analytical, finite element and experimental study of single-lap joints bonded with epoxy adhesive

Marcin Kujawa[1], Łukasz Smakosz[1], Piotr Paczos[2], Faizullah Jan[1], Karol Winkelmann[1], Violetta Konopińska-Zmysłowska[1], Victor A. Eremeyev[3]

- The paper presents closed-form analytical solutions for the stress distribution in tensile-loaded single-lap joints with a realistically thin adhesive layer.
- One of the proposed analytical model captures both shear and peel stresses in the adhesive layer.
- The accuracy of the analytical solutions is assessed by comparison with other analytical models, FEM analysis and experimental tests.

An analytical, finite element and experimental study of single-lap joints bonded with epoxy adhesive

Marcin Kujawa[1], Łukasz Smakosz[1], Piotr Paczos[2], Faizullah Jan[1], Karol Winkelmann[1], Violetta Konopińska-Zmysłowska[1], Victor A. Eremeyev[3]

[1]*Gdańsk University of Technology*
G. Narutowicza 11/12, 80-233 Gdańsk Poland
[2]*Poznań University of Technology*
Jana Pawla II 24, 61-139 Poznań Poland
[3]*University of Cagliari*
Via Marengo 2, 09123 Cagliari Italy

Abstract

This paper investigates the stress distribution in tensile-loaded single-lap joints made of aluminum and bonded with an epoxy adhesive using analytical modeling, finite element analysis (FEM), and experimental testing. The analytical framework is developed for joints with varying material properties, adherend and adhesive thicknesses, and overlap lengths, assuming a constant joint width and a thin adhesive layer. The analysis is based on elasticity theory and the principle of stationary potential energy. Three closed-form solutions are derived. Solutions I and II describe shear stress transfer at the interface, neglecting and including transverse deformability of the adhesive, respectively. Solution III further extends the formulation by accounting for joint bending induced by load eccentricity, enabling the evaluation of both shear and peel stresses. The proposed solutions are validated against classical analytical models (Goland & Reissner, Hart-Smith), FEM simulations (Abaqus), and experimental results. Owing to the adopted representation of the adhesive layer, the stresses predicted by Solution III should be interpreted as effective structural stresses rather than exact local adhesive stresses, particularly near the overlap edges, where the stress field is influenced by the combined effect of geometric features and material mismatch, leading to a singularity. In this region, not only the stress magnitude but also the precise location of extreme values becomes inherently ambiguous and method-dependent. Despite these limitations, Solution III provides a physically consistent representation of the stress state in the joint, accurately capturing the global stress distribution and providing reliable

estimates of extreme stress levels.

Keywords: single-lap joints, closed-form analytical solutions, stationary potential energy principle, FEM, experimental tests

---

Nomenclature and symbols

x	longitudinal coordinate along the joint
y	transverse coordinate (joint width direction)
z	through-thickness coordinate
l	overlap length
l_i	distance from the support to the start of the overlap ($i = 1, 2$ adherends)
b	joint width
t_i	thickness of layer i ($i = 1, 2$ adherends; $i = 3$ adhesive)
P	applied tensile force
E_i	Young's modulus of layer i
G_i	shear modulus of layer i
ν_i	Poisson's ratio of layer i
σ	normal stress
τ	shear stress
ϵ	normal strain
γ	shear strain
$\sigma_i(x)$	axial normal stress in layer i ($i = 1, 2$ adherends)
$\tau_3(x)$	shear stress in the adhesive layer
$\sigma_3(x)$	peel stress in the adhesive layer
D_i	bending stiffness of adherend i ($i = 1, 2$ adherends)
D_0	bending stiffness of the overlap region
D_b	total bending stiffness of the adherends
K_s	effective (approximate) shear stiffness per unit length of the adhesive layer
d	neutral axis offset of the joint cross-section
k	bending coefficient accounting for load eccentricity
s_{max}	maximum interlayer slip
δ_s	relative slip index
η	dimensionless bending-shear interaction parameter
V	total strain energy
V_{10}	strain energy density of adherend 1

V_{20} strain energy density of adherend 2
V_{30} strain energy density of the adhesive layer

1. Introduction

Among the various types of adhesive joints used in engineering (Fig. 1), the most common and conventional configuration is the single-lap joint (Fig. 2). One of the earliest studies on single-lap joints was conducted by Volkersen, whose seminal work was published in 1938 [1]. In his analytical model, developed originally in the context of riveted joints, Volkersen introduced a non-uniform distribution of shear stresses in joints subjected to axial tensile loading. This approach stood in contrast to earlier, more simplified model, which assumed a constant shear stress distribution within the adhesive layer. As de Bruyne later pointed out [2], single-lap joints are prone to deformation. The actual deformation depends not only on the shear deformation of the adhesive – governed by its shear modulus – but also on the deformation of the adherends. Moreover, and most importantly, such joints tend to bend due to the eccentricity of the tensile load path. In the same year, 1944 – prior to the publication of de Bruyne's paper – Goland & Reissner proposed an analytical solution that accounted not only for shear stresses in the adhesive but also for peel stresses in the joint [3]. Due to the complexity of the resulting formulation, they simplified the model by assuming that the adherends were of equal thickness and made of the same material. In the following years, numerous papers and technical reports were published addressing the problem of single-lap joints [4, 5, 6, 7, 8, 9, 10, 11, 12]. Among them, the papers by Adams and his co-authors [13, 14, 15] deserve special attention, as they provide clear and general analytical solutions to the problem – not only along the load axis but also in the transverse direction – although, unfortunately, they do not account for peel stresses in the joint. Next, a more general and comprehensive analytical solution was developed by Cheng, Chen, and Shi [16]. Initially, Chen and Cheng formulated the problem in a manner similar to that of Goland & Reissner [17]. They subsequently introduced a general linear analytical solution based on the energy approach, accounting for adherends of different thicknesses, made of various materials, while assuming a thin adhesive layer. However, the authors of the study [16], following the approach of Goland & Reissner, assumed symmetry in the peel stress distribution within the joint under bending. As a result, the analytical solution was formulated using a coordinate system located at the center of the single-lap joint. Nevertheless, extreme peel stresses do not occur at the mid-thickness of the adhesive layer but are typically asymmetrical and arise at the interfaces between the adhesive

and the adherends. The solution proposed in this paper seeks to address this issue, among other things, and represents a further development and refinement of precisely these linear analytical formulations. Further analytical studies were published in subsequent years [18, 19, 20, 21, 22, 23, 24, 25, 26, 27, 28, 29, 30]. At this point, it is important to distinguish between two traditional approaches to analyzing the mechanical behavior of bonded joints. The first approach, outlined above and adopted in the present study, is based on evaluating stress distributions within the joint under the assumptions of linear elasticity. The second, more recent approach is founded on the principles of fracture mechanics. As noted above, numerous analytical formulations have been proposed over the years to describe the mechanical behavior of bonded joints. Important milestones in the description of the development of analytical models are the papers of da Silva et al. [31], Wang and Zhang [32], and Du et al. [33]. Together, these contributions have played a significant role in advancing the analytical modeling of bonded joints.

In many analytical models of adhesively bonded joints, the stress analysis is performed using simplified two-dimensional, linear-elastic formulations. These assumptions make it possible to obtain closed-form solutions and provide a convenient basis for engineering assessment. In a large class of such approaches, the adhesive layer is represented in an averaged sense, often through elastic type idealizations. This significantly reduces the complexity of the governing equations while still capturing the main features of load transfer between the adherends. However, these simplified representations do not explicitly resolve the detailed stress state within the adhesive layer. In particular, the variation of stresses across the adhesive thickness and the differences between the two adherend-adhesive interfaces are only approximately described. As a result, the equilibrium conditions at the the interfaces, as well as the local stress concentrations associated with bending and transverse deformation effects, are represented in a simplified manner. In single-lap joints, the eccentric load path induces bending of the adherends and gives rise to asymmetric peel stress distributions, with peak values typically occurring at the adhesive-adherend interfaces. Accurately capturing this coupled bending-shear behavior and the associated asymmetric interfacial stress state within a closed-form analytical framework, while maintaining general applicability and analytical tractability, therefore remains a challenging problem.

Substantial progress has been achieved through numerical formulations and computational modeling, with particular emphasis on the FEM [34, 35, 36, 37, 38]. In parallel, experimental investigations have accompanied these theoretical and numerical developments since the earliest studies, providing validation and deeper insight into the mechanical behavior of bonded joints [2, 39, 40, 41, 42, 43, 44].

FEM numerical simulations, together with supporting experimental studies, have been primarily applied to advanced bonded-joint configurations and complex loading conditions, for which closed-form analytical descriptions are excessively complicated or not feasible.

Despite the substantial amount of research conducted in this field, certain aspects of existing analytical or FEM solutions still exhibit limitations, even within strictly linear analytical frameworks. The need for further research is further emphasized by the ongoing development of advanced adhesive materials and innovative structural designs across a wide range of engineering applications, including aerospace, automotive, and civil engineering. Consequently, targeted analytical studies, FEM simulations, and experimental investigations remain still necessary to evaluate and support existing design approaches for various structures. The aim of this study is to contribute to these efforts by comparing the authors' proposed analytical solutions with selected classical analytical solutions that serve as points of reference. The results are then verified using the FEM and experimental research.

Thus, the novelty of this study lies in the development of an extended analytical framework for single-lap bonded joints, formulated within a general linear-elastic approach and explicitly accounting for both shear and bending effects in a realistically thin adhesive layer. A key contribution is the derivation of new closed-form expressions for the bending coefficients - denoted as k for symmetric adherents and k_1, k_2 for asymmetric adherents - which enable the prediction of bending moments in joints with arbitrary geometric and material configurations. Although bending effects have been addressed in the classical formulations of Goland & Reissner, Hart-Smith, and Cheng, Chen, and Shi, the formulation presented here provides an alternative and more general treatment.

The paper also introduces a method for solving the coupled differential equations that describe the behavior of a joint subjected to eccentric tensile loading. As mentioned above, proposed theoretical developments are complemented by a consistent verification strategy that combines FE simulations with experimental tests on aluminum-epoxy joints bonded using 3M™ Scotch-Weld™ DP490 adhesive.

The most general formulation developed in the present paper (Solution III) is intended to complement existing analytical approaches by extending the description of the coupled bending-shear behavior of single-lap joints. The solution is derived from the principle of stationary potential energy and provides a fully coupled representation of axial forces, shear forces, and bending moments in the joint. This enables the simultaneous evaluation of shear and peel stresses associated with the interaction between the adherends. At the same time, the adhesive layer is described in an energetically equivalent, averaged manner rather than through a de-

tailed three-dimensional constitutive model. The formulation therefore captures the global load-transfer mechanisms and the interfacial stress measures most relevant for structural assessment, while the detailed through-thickness stress distribution in the adhesive is not resolved explicitly.

The proposed model (Solution III) captures the asymmetric bending response of single-lap joints and the associated non-symmetric peel stress fields observed in numerical and experimental results, while remaining suitable for practical analysis. The overlap is described using an effective composite-beam assumption, with its validity governed by a dimensionless parameter η relating adhesive shear stiffness to adherend bending stiffness. The model is applicable for sufficiently slender adherends ($t/l \ll 1$) and for an admissible range of adhesive thickness t_3, which ensures both the validity of the thin-layer assumption and a physically meaningful shear transfer mechanism along the overlap. Due to the presence of a stress singularity at the overlap edge, the stress field in its immediate vicinity is not physically representative. Therefore, stresses are evaluated at a finite distance from the edge. To this end, a reference distance l_e is introduced to characterize the extent of the edge-effect zone. This distance, dependent on the geometric characteristics of the joint and the material contrast between its components, defines an exclusion region within which the singular behavior dominates, ensuring that the reported stresses reflect the global load transfer rather than local singular effects.

The original contributions of this work can be summarized as follows:

(i) development of a novel closed-form analytical solution (Solution III) that consistently captures coupled shear–bending behavior in single-lap joints,

(ii) derivation of new expressions for bending coefficients applicable to both symmetric and asymmetric configurations,

(iii) formulation of a unified framework enabling evaluation of effective structural stresses in the presence of edge singularities,

(iv) comprehensive validation through FEM simulations and experimental measurements.

2. Analytical solutions

Energy methods constitute one of the most effective and widely applied analytical approaches in structural mechanics, as well as in the theories of elasticity and plasticity of mechanical systems [45]. Owing to their versatility and strong theoretical foundations, these methods form the basis of the present study, which focuses on the development of analytical models for bonded lap joints. The application of the energy approach enables the derivation of closed-form solutions

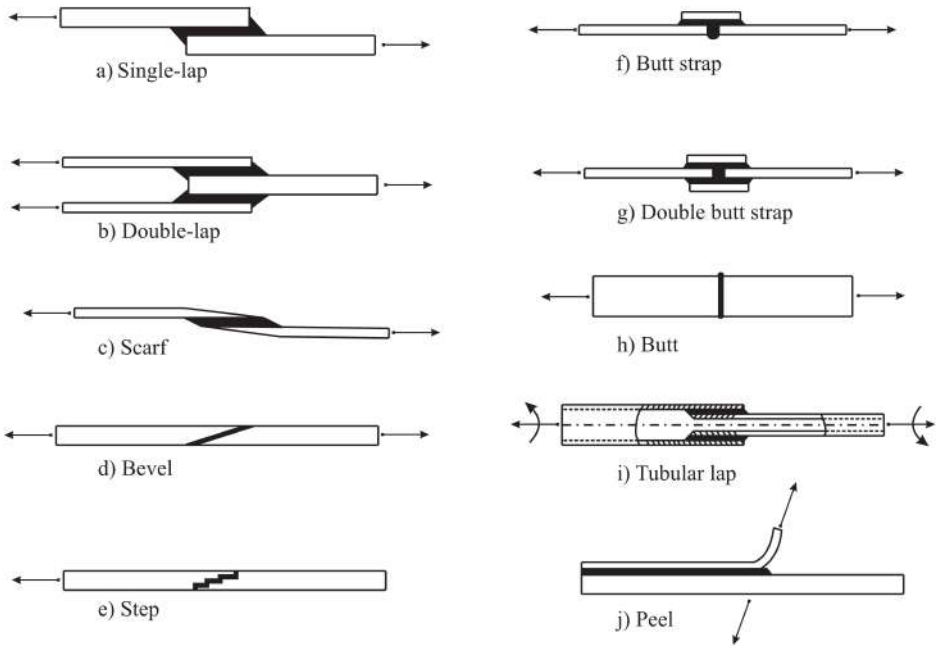

Figure 1: Typical examples of engineering adhesive joints.

that provide a rapid and effective means of preliminary assessment of the stress distribution within the joint while ensuring clarity and physical interpretability. This paper presents three analytically formulated solutions that progressively capture increasing levels of mechanical complexity in the behavior of bonded lap joints. The first model (Solution I) neglects shear deformations in the adherends but includes them in the adhesive layer, providing a simplified yet sufficiently accurate approximation. The second model (Solution II) extends the formulation by incorporating shear deformations in the adherends, resulting in a more accurate representation of the joint response. Finally, the third and most comprehensive model in this study (Solution III) accounts for bending effects and the associated joint peeling stress caused by the eccentricity of the applied tensile force. As noted earlier, all proposed analytical models were derived using the energy approach, in which the total deformation energy V is expressed as follows:

$$V = \int \int \int V_0 \, \mathrm{d}x \, \mathrm{d}y \, \mathrm{d}z, \tag{1}$$

where local elastic stress-strain energy V_0 is defined as:

$$V_0 = \frac{1}{2} \left(\sigma_x \epsilon_x + \sigma_y \epsilon_y + \sigma_z \epsilon_z + \tau_{xy} \gamma_{xy} + \tau_{yz} \gamma_{yz} + \tau_{xz} \gamma_{xz} \right), \tag{2}$$

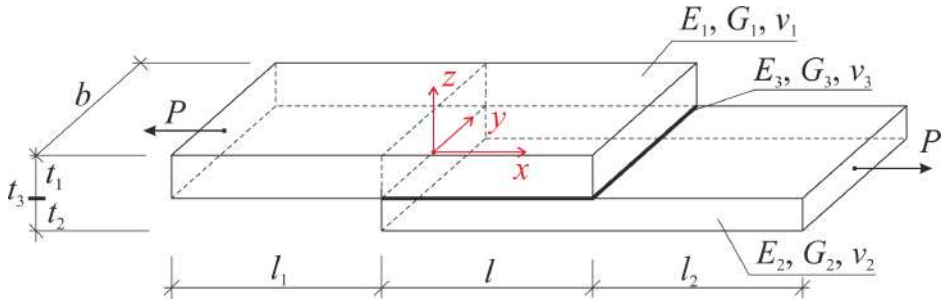

Figure 2: Schematic representation and notation of the single-lap joint.

which, considering Hooke's law, can be expressed solely in terms of normal and shear stresses as follows:

$$V_0 = \frac{1}{2E}\left(\sigma_x^2 + \sigma_y^2 + \sigma_z^2\right) - \frac{\nu}{E}\left(\sigma_x\sigma_y + \sigma_y\sigma_z + \sigma_z\sigma_x\right) + \ldots + \frac{1}{2G}\left(\tau_{xy}^2 + \tau_{yz}^2 + \tau_{xz}^2\right), \tag{3}$$

where E is Young's modulus, ν is Poisson's ratio, and G is the shear (Kirchhoff) modulus.

By employing variational methods and the principle of stationary potential energy, $\delta V = 0$, the differential equations and corresponding closed-form solutions are obtained for each case analyzed [46]. It should be emphasized that all formulations rely on the assumption of a physically realistic adhesive layer that is sufficiently thin to justify the adopted analytical simplifications.

2.1. Solution I: Analytical model neglecting shear deformations in the adherends

To solve the problem of shear in a single-lap joint (Fig. 2), while neglecting shear deformations in the adherends and considering them only in the adhesive layer, several simplifying assumptions were adopted. The material is assumed to be linearly elastic and isotropic. The adhesive layer undergoes only shear deformation, whereas the adherends are subjected exclusively to axial (tensile) deformation. The adhesive layer is assumed to be thin, and bending effects are neglected. Moreover, a uniform stress distribution across the entire width of the joint is assumed. In this case, the strain energy of the joint is given by:

$$V = \int\int\int \left(V_{10} + V_{20} + V_{30}\right)\, \mathrm{d}x\, \mathrm{d}y\, \mathrm{d}z, \tag{4}$$

where the local elastic strain-energy components of the individual elements (1 - upper adherend, 2 - lower adherend, 3 - adhesive) are expressed in terms of stress as follows:

$$V_{10} = \frac{1}{2E_1}\sigma_1^2(x), \quad V_{20} = \frac{1}{2E_2}\sigma_2^2(x), \quad V_{30} = \frac{1}{2E_3}\left[2(1+\nu_3)\tau_3^2(x)\right], \tag{5}$$

where E_1 and E_2 are the Young's moduli of the top and bottom adherends, respectively, and E_3 and ν_3 are the material constants describing the adhesive along the length of the joint (x-axis).

The following relation is then obtained:

$$V_{S_I} = b\left[\int_{-\frac{t_1}{2}}^{\frac{t_1}{2}}\int_0^l V_{10}\,\mathrm{d}x\,\mathrm{d}z + \int_{-\frac{t_2}{2}}^{\frac{t_2}{2}}\int_0^l V_{20}\,\mathrm{d}x\,\mathrm{d}z + t_3\int_0^l V_{30}\,\mathrm{d}x\right], \tag{6}$$

where t_1 and t_2 are the thicknesses of the top and bottom adherends, respectively, t_3 is the thickness of the adhesive, l and b is the length and the width of the joint, respectively.

After integrating along the joint width b, one obtains:

$$V_{S_I} = \frac{b}{2}\int_0^l \left(\frac{\sigma_1^2(x)}{E_1}t_1 + \frac{\sigma_2^2(x)}{E_2}t_2 + \frac{\tau_3^2(x)}{G_3}t_3\right)\mathrm{d}x, \tag{7}$$

and, after basic transformations, in which $\sigma_2(x)$ and $\tau_3(x)$ are expressed in terms of $\sigma_1(x)$, the strain energy can be written in the form:

$$V_{S_I} = \frac{b}{2}\int_0^l \left[\frac{t_1^2 t_3}{G_3}\sigma_1'^2(x) + \left(\frac{t_1}{E_1} + \frac{t_1^2}{E_2 t_2}\right)\sigma_1^2(x) - \frac{2Pt_1}{bE_2t_2}\sigma_1(x) + \frac{P^2}{b^2E_2t_2}\right]\mathrm{d}x, \tag{8}$$

where P is the tensile force applied to the joint.

In the transformations from (7) to (8), the following relationships derived from equilibrium conditions are used:

$$\sigma_1(x)t_1 + \sigma_2(x)t_2 = \frac{P}{b}, \quad \tau_3(x) = t_1\sigma_1'(x). \tag{9}$$

The relations in (9) are derived by assuming force equilibrium in the joint. Additionally, based on Fig. 3, assuming that $\tau_1(x) = \tau_3(x)$ at the lower surface of the upper adherend ($z = 0$), the relationship between the normal stress and shear stresses is given by:

$$t_1\sigma_1(x) + \tau_1(x)dx = t_1\sigma_1(x) + t_1 d\sigma_1(x), \tag{10}$$

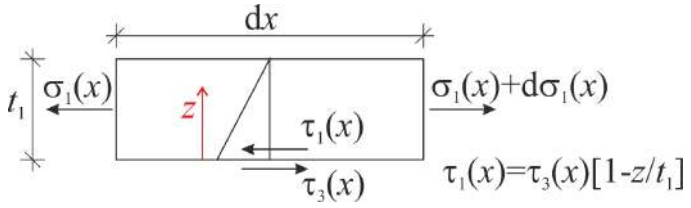

Figure 3: Shear stress distribution on the top adherend joint section.

$$\tau_1(x) = t_1 \frac{\sigma_1(x)}{dx} = t_1 \sigma_1'(x) \longrightarrow \tau_3(x) = t_1 \sigma_1'(x). \tag{11}$$

Next, using the principle of stationary potential energy and variational calculus, one obtains the Euler-Lagrange differential equation:

$$\frac{2t_1^2 t_3}{G_3}\sigma_1''(x) - \frac{2t_1 t_2 E_2 + 2t_1^2 E_1}{t_2 E_1 E_2}\sigma_1(x) + \frac{2Pt_1}{bt_2 E_2} = 0, \tag{12}$$

and the corresponding solution:

$$\sigma_1(x) = \frac{P}{b}\psi + C_1 e^{x\sqrt{\alpha}} + C_2 e^{-x\sqrt{\alpha}} \tag{13}$$

where $\alpha = \frac{G_3(E_1 t_1 + E_2 t_2)}{t_3 E_1 t_1 E_2 t_2}$, $\psi = \frac{E_1}{E_1 t_1 + E_2 t_2}$ and C_1, C_2 are constants that can be determined from boundary conditions of the form:

$$\begin{aligned} x = 0, \quad & \sigma_1(x=0) = \tfrac{P}{bt_1}, \\ x = l, \quad & \sigma_1(x=l) = 0, \end{aligned} \tag{14}$$

$$C_1 = -\frac{P\left(t_1\psi e^{l\sqrt{\alpha}} - t_1\psi + 1\right)}{b\left(e^{2l\sqrt{\alpha}} - 1\right)t_1}, C_2 = -\frac{Pe^{l\sqrt{\alpha}}\left(-e^{l\sqrt{\alpha}} + t_1\psi e^{l\sqrt{\alpha}} - t_1\psi\right)}{b\left(e^{2l\sqrt{\alpha}} - 1\right)t_1}. \tag{15}$$

After substituting the constants C_1 and C_2 into Eq. (8), one obtains the normal stress distribution in the top adherend:

$$\sigma_1(x) = \frac{P}{b}\psi\left\{1 + \frac{1-\psi t_1}{\psi t_1}\frac{\sinh[(l-x)\sqrt{\alpha}]}{\sinh[l\sqrt{\alpha}]} - \frac{\sinh[x\sqrt{\alpha}]}{\sinh[l\sqrt{\alpha}]}\right\}, \tag{16}$$

and the corresponding shear-stress distribution in the adhesive is given by:

$$\tau_3(x) = t_1\sigma_1'(x) = -\frac{P}{b}\sqrt{\alpha}\left\{(1-\psi t_1)\frac{\cosh[(l-x)\sqrt{\alpha}]}{\sinh[l\sqrt{\alpha}]} + \psi t_1\frac{\cosh[x\sqrt{\alpha}]}{\sinh[l\sqrt{\alpha}]}\right\}. \quad (17)$$

The analytical expression (17), which describes the shear-stress distribution in the adhesive layer, corresponds to the solution originally proposed by Volkersen [1], later independently derived by Sazhin [47], and subsequently examined by Adams [13].

2.2. Solution II: Analytical model including shear deformations in the adherends

In the second formulation, which incorporates shear deformations in the adherends, the derivation follows an approach analogous to that used in the Solution I. As a result, the local elastic strain-energy components take the following form:

$$\begin{aligned} V_{10} &= \frac{1}{2E_1}\left[\sigma_1^2(x) + 2(1+\nu_1)\tau_1^2(x)\right], \\ V_{20} &= \frac{1}{2E_2}\left[\sigma_2^2(x) + 2(1+\nu_2)\tau_2^2(x)\right], \\ V_{30} &= \frac{1}{2E_3}\left[2(1+\nu_3)\tau_3^2(x)\right]. \end{aligned} \quad (18)$$

After integrating over the joint width and applying (4), one obtains:

$$V_{S_{II}} = \frac{b}{2}\int_0^l \left\{\left[\frac{\sigma_1^2(x)}{2E_1} + \frac{\tau_1^2(x)}{2G_1}\right]t_1 + \left[\frac{\sigma_2^2(x)}{2E_2} + \frac{\tau_2^2(x)}{2G_2}\right]t_2 + \frac{\tau_3^2(x)}{G_3}t_3\right\}\mathrm{d}x \quad (19)$$

By applying transformations analogous to those used in Solution I, the strain-energy expression can be written as:

$$V_{S_{II}} = \frac{b}{2}\int_0^l \left[\left(\frac{t_1^3}{2G_1} + \frac{t_1^2t_2}{2G_2} + \frac{t_1^2t_3}{G_3}\right)\sigma_1'^2(x) + \left(\frac{t_1}{E_1} + \frac{t_1^2}{E_2t_2}\right)\sigma_1^2(x) + ... - \frac{2Pt_1}{bE_2t_2}\sigma_1(x) + \frac{P^2}{b^2E_2t_2}\right]\mathrm{d}x \quad (20)$$

Next, by applying variational methods, the Euler-Lagrange differential equation is obtained:

$$\frac{t_1^2(t_1G_2G_3 + G_1G_3t_2 + 2t_3G_1G_2)}{G_1G_2G_3}\sigma_1''(x) - \frac{2t_1t_2E_2 + 2t_1^2E_1}{t_2E_1E_2}\sigma_1(x) + \frac{2Pt_1}{bt_2E_2} = 0, \quad (21)$$

where the form of the stress function is nearly the same as that in Solution I:

$$\sigma_1(x) = \frac{P}{b}\psi + C_1 e^{x\sqrt{\beta}} + C_2 e^{-x\sqrt{\beta}}, \tag{22}$$

The only difference is that the constant α is replaced by β, defined as: $\beta = \frac{2G_1G_2G_3(E_1t_1+E_2t_2)}{E_1E_2t_1t_2(G_2G_3t_1+G_1G_3t_2+2G_1G_2t_3)}$. The constants C_1 and C_2 have the same form as in Solution I and are determined using the same boundary conditions (14), with α replaced by β:

$$C_1 = -\frac{P\left(t_1\psi e^{l\sqrt{\beta}} - t_1\psi + 1\right)}{b\left(e^{2l\sqrt{\beta}} - 1\right)t_1}, C_2 = -\frac{Pe^{l\sqrt{\beta}}\left(-e^{l\sqrt{\beta}} + t_1\psi e^{l\sqrt{\beta}} - t_1\psi\right)}{b\left(e^{2l\sqrt{\beta}} - 1\right)t_1}. \tag{23}$$

As before, the solution yields the normal-stress distribution in the adherend:

$$\sigma_1(x) = \frac{P}{b}\psi\left\{1 + \frac{1-\psi t_1}{\psi t_1}\frac{\sinh[(l-x)\sqrt{\beta}]}{\sinh[l\sqrt{\beta}]} - \frac{\sinh[x\sqrt{\beta}]}{\sinh[l\sqrt{\beta}]}\right\}, \tag{24}$$

and the corresponding shear-stress distribution in the adhesive:

$$\tau_3(x) = t_1\sigma_1'(x) = -\frac{P}{b}\sqrt{\beta}\left\{(1-\psi t_1)\frac{\cosh[(l-x)\sqrt{\beta}]}{\sinh[l\sqrt{\beta}]} + \frac{\psi t_1\cosh[x\sqrt{\beta}]}{\sinh[l\sqrt{\beta}]}\right\}. \tag{25}$$

The analytical expression (25), which characterizes the shear-stress distribution in the adhesive layer, is consistent with the solution presented and examined by Adams [13] in the context of an analytical model that incorporates shear deformations in the adherends. This formulation provides a more accurate representation of the joint's mechanical behavior than the simplified model that neglects shear deformation in the adherends. Goland & Reissner [3], with further elaboration by Sneddon [48], demonstrated – based on strain-energy analysis – that shear deformations in the adherends may be neglected relative to those in the adhesive layer only if the condition $\frac{t_1G_3}{t_3G_1} \leq 0.1$ is satisfied.

The classical formulations presented in Solutions I and II neglect the fundamental deformation that a single-lap joint typically experiences, namely bending. Therefore, a key part of this study was devoted to developing a more comprehensive model that incorporates the influence of bending while generalizing the formulation so that all geometric and material parameters can be freely modified, subject to two restrictions: elastic material behavior and a thin adhesive layer.

Numerical examples corresponding to Solutions I and II are presented in the Figs. 16 and 17 in section Numerical examples.

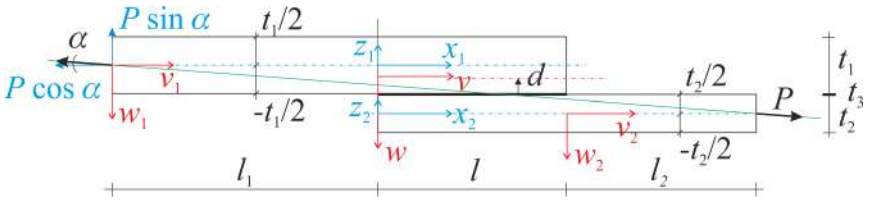

Figure 4: Coordinate systems of the parts of the joint.

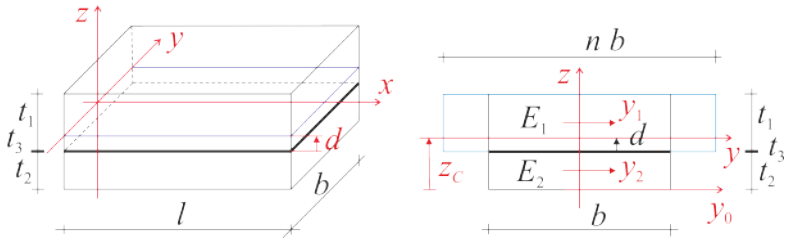

Figure 5: Detailed view of the overlap region.

2.3. *Solution III: Comprehensive analytical model incorporating bending-induced peeling*

After a detailed – yet, in the authors' view, necessary – introduction aimed at presenting the energy-based approach through simple but essential cases, the analysis now turns to the main analytical solution. In this formulation, the joint is assumed to undergo bending during tensile loading, which results in the development of peel stresses in the adhesive layer in addition to shear stresses. In this approach, the potential energy of the joint is expressed through the local components of the elastic strain energy written in terms of stresses:

$$V_{10} = \frac{1}{2\overline{E}_1}\left\{\sigma_{1x}^2(x,z_1) + \sigma_{1z}^2(x,z_1) - 2\overline{\nu}_1\sigma_{1x}(x,z_1)\sigma_{1z}(x,z_1) + 2[1+\overline{\nu}_1]\tau_{1zx}^2(x,z_1)\right\},$$

$$V_{20} = \frac{1}{2\overline{E}_2}\left\{\sigma_{2x}^2(x,z_2) + \sigma_{2z}^2(x,z_2) - 2\overline{\nu}_2\sigma_{2x}(x,z_2)\sigma_{2z}(x,z_2) + 2[1+\overline{\nu}_2]\tau_{2zx}^2(x,z_2)\right\}, \tag{26}$$

$$V_{30} = \frac{1}{2\overline{E}_3}\left\{\sigma_{3z}^2(x) + 2[1+\overline{\nu}_3]\tau_{3zx}^2(x)\right\}.$$

where $\overline{E}_i = \frac{E_i}{1-\nu_i^2}$, $\overline{G}_i = \frac{\overline{E}_i}{2(1+\overline{\nu}_i)}$, and $\overline{\nu}_i = \frac{\nu_i}{1-\nu_i}$ for i=1, 2, 3, assuming that the materials are in a two-dimensional state, and where $\overline{\nu}_i$ denotes the effective Poisson's

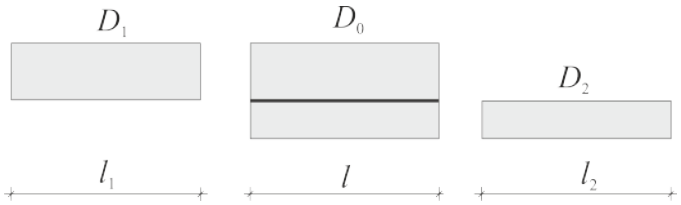

Figure 6: View of the individual parts of the joint in relation to their stiffness.

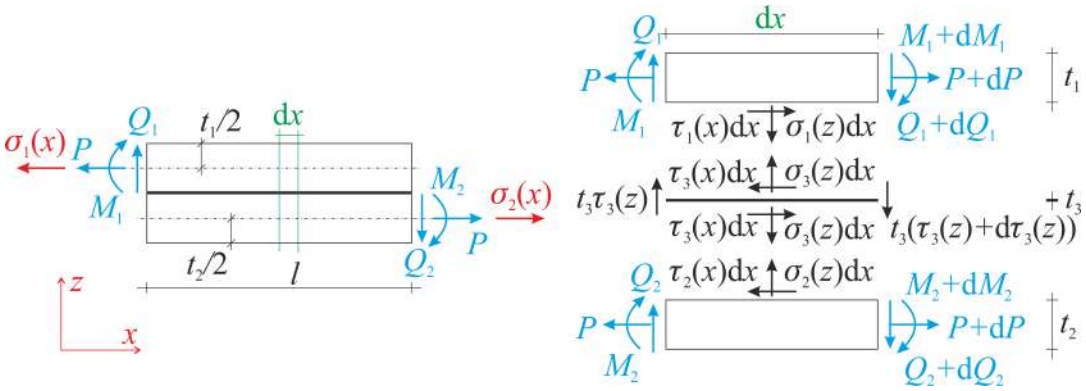

Figure 7: Equilibrium state of internal forces and stresses in the joint.

ratio under plane-strain conditions.

After integrating over the width of the joint, as shown Fig. 5, we obtain:

$$V_{S_{III}} = b\left[\int_{-\frac{t_1}{2}}^{\frac{t_1}{2}}\int_0^l V_{10}\,\mathrm{d}x\,\mathrm{d}z_1 + \int_{-\frac{t_2}{2}}^{\frac{t_2}{2}}\int_0^l V_{20}\,\mathrm{d}x\,\mathrm{d}z_2 + t_3\int_0^l V_{30}\,\mathrm{d}x\right] \tag{27}$$

Next, taking into account the differing material properties of the adherends, it is necessary to determine the position of the neutral axis of the joint, as illustrated in Figs. 4, 5. The position of the neutral axis d is given by:

$$d = z_C - t_2 = \frac{nt_1^2 - t_2^2}{2(nt_1 + t_2)} \tag{28}$$

where $z_C = \frac{t_2^2+nt_1(t_1+2t_2)}{2(nt_1+t_2)}$ and $n = \frac{\overline{E}_1}{\overline{E}_2}$.

This, in turn, allows the bending stiffness of the individual joint components to be

determined, as shown in Fig. 6:

$$
\begin{aligned}
D_1 &= \frac{1}{12}\overline{E}_1\, b\, t_1^3, \\
D_0 &= \frac{2b}{3}\left\{\overline{E}_1\left[(t_1-d)^3+d^3\right]+\overline{E}_2\left[(t_2+d)^3-d^3\right]\right\}, \\
D_2 &= \frac{1}{12}\overline{E}_2\, b\, t_2^3.
\end{aligned}
\tag{29}
$$

It is very important at this point to note that formulas (28) and (29) are derived under the assumption of perfect kinematic compatibility between the bonded layers, implying identical longitudinal strains and a common elastic line. This assumption is introduced to obtain a tractable closed-form expression for the global flexural rigidity of the bonded structure and corresponds to the classical effective-beam approach commonly employed in the analysis of layered and adhesively bonded beams when the emphasis is placed on the global bending response rather than on the detailed local stress state. The adhesive layer is assumed to be thin relative to the thicknesses of the bonded load-bearing layers. Under this assumption, relative longitudinal displacements between the layers are significantly constrained and the bending behavior of the structure approaches that of a monolithic beam in an average energetic sense even when the elastic properties of the adhesive differ from those of the adherends. Consequently, the proposed formulation yields an approximation of the global bending stiffness and the position of the neutral axis while avoiding the additional complexity associated with more refined layered or shear-deformation models. Such effects however lie beyond the scope of the present work which is restricted to the investigation of the global bending behavior of the bonded structure. Within the framework of the classical Bernoulli beam theory adopted herein the normal stress component in the thickness direction z is derived consistently with the assumed kinematics and equilibrium conditions. It should therefore be interpreted as an effective stress measure resulting from the adopted beam-level description rather than as a fully resolved three-dimensional stress component, since the Bernoulli approximation is employed as a kinematic constraint for the derivation of the overall bending response and not as a detailed three-dimensional model of the adhesive layer; accordingly, this assumption is not intended to reproduce the local interfacial kinematics near the overlap edge, but rather to provide a consistent description of the global structural response.

By establishing the equilibrium of the internal forces, as illustrated in Fig. 7, the values of the bending moments M_1 and M_2 – which depend on the coefficients k_1

and k_2 – can be determined:

$$Q_1 = Q_2 = \frac{1}{l}\left[P\left(\frac{t_1}{2} + \frac{t_2}{2}\right) - M_1 - M_2\right], \tag{30}$$

where $M_1 = k_1 \frac{P\, t_1}{2}$, $M_2 = k_2 \frac{P\, t_2}{2}$. The bending moments in the three segments of the joint, as shown in Fig. 4, can be described as follows:

$$\begin{aligned}
M_1^* &= P\,\alpha\, v_1 - P\, w_1(v_1) \quad \text{at} \quad 0 \le v_1 \le l_1, \\
M_0^* &= P\,\alpha\,(l_1 + v) - P\left[\frac{t_1}{2} + w(v) - d\right] \quad \text{at} \quad 0 \le v \le l, \\
M_2^* &= P\,\alpha\left(l_1 + l + v_2\right) - P\left[\frac{t_1}{2} + \frac{t_2}{2} + w_2(v_2)\right] \quad \text{at} \quad 0 \le v_2 \le l_2,
\end{aligned} \tag{31}$$

where $\alpha = \tan[\alpha] = \frac{t_1+t_2}{2(l_1+l+l_2)}$, $\sin[\alpha] = \alpha$, and $\cos[\alpha] = 1$.
Assuming small rotations (i.e., small displacements), three differential equations can be formulated, with their solutions given by:

$$\begin{aligned}
w_1''(v_1) &= -\frac{M_1^*}{D_1} \rightarrow w_1(v_1) = \alpha\, v_1 + e^{\frac{v_1\sqrt{P}}{\sqrt{D_1}}} W_1 + e^{-\frac{v_1\sqrt{P}}{\sqrt{D_1}}} W_2, \\
w''(v) &= -\frac{M_0^*}{D_0} \rightarrow w(v) = \alpha(l_1 + v) + d - \frac{t_1}{2} + e^{\frac{v\sqrt{P}}{\sqrt{D_0}}} W_3 + e^{-\frac{v\sqrt{P}}{\sqrt{D_0}}} W_4, \\
w_2''(v_2) &= -\frac{M_2^*}{D_2} \rightarrow w_2(v_2) = \alpha(l_1 + l + v_2) - \frac{t_1 + t_2}{2} + e^{\frac{v_2\sqrt{P}}{\sqrt{D_2}}} W_5 + e^{-\frac{v_2\sqrt{P}}{\sqrt{D_2}}} W_6.
\end{aligned} \tag{32}$$

The constants W_1 through W_6 can be determined from the boundary conditions:

$$\begin{aligned}
&w_1(v_1 = 0) = 0, \\
&w_1(v_1 = l_1) = w(v = 0), \\
&w_1'(v_1 = l_1) = w'(v = 0), \\
&w(v = l) = w_2(v_2 = 0), \\
&w'(v = l) = w_2'(v_2 = 0), \\
&w_2(v_2 = l_2) = 0.
\end{aligned} \tag{33}$$

The constants W_1 through W_6, which result from these assumptions, are provided in the Digital appendix due to their complexity (https://drive.pg.edu.pl/s/bUwBtzGuG3BqnDk).

By determining the forms of the functions $w_1(v_1)$ and $w_2(v_2)$, along with their second derivatives, one can obtain the moments M_1, M_2, and the coefficients k_1 and k_2 from the following relationships:

$$M_1 = -D_1 w_1''(v_1)\Big|_{v_1=l_1}, \qquad (34)$$
$$M_2 = -D_2 w_2''(v_2)\Big|_{v_2=0}.$$

$$k_1 = \frac{\sqrt{D_1}\sinh(\beta_1)}{t_1(\zeta+\xi)}\left\{\sqrt{D_0}\left[t_2+2d+(t_1-2d)\cosh(\beta_0)\right]\cosh(\beta_2)+... \right.$$
$$\left.+\sqrt{D_2}(t_1-2d)\sinh(\beta_0)\sinh(\beta_2)\right\}, \qquad (35)$$

$$k_2 = \frac{\sqrt{D_2}\sinh(\beta_2)}{t_2(\zeta+\xi)}\left\{\sqrt{D_0}\left[t_1-2d+(t_2+2d)\cosh(\beta_0)\right]\cosh(\beta_1)+... \right.$$
$$\left.+\sqrt{D_1}(t_2+2d)\sinh(\beta_0)\sinh(\beta_1)\right\}. \qquad (36)$$

where $\beta_1 = l_1\sqrt{\frac{P}{D_1}}$, $\beta_0 = l\sqrt{\frac{P}{D_0}}$, $\beta_2 = l_2\sqrt{\frac{P}{D_2}}$, and

$$\zeta = \cosh(\beta_1)\left[D_0\cosh(\beta_2)\sinh(\beta_0)+\sqrt{D_0}\sqrt{D_2}\cosh(\beta_0)\sinh(\beta_2)\right], \qquad (37)$$

$$\xi = \sqrt{D_1}\sinh(\beta_1)\left[\sqrt{D_0}\cosh(\beta_0)\cosh(\beta_2)+\sqrt{D_2}\sinh(\beta_0)\sinh(\beta_2)\right], \qquad (38)$$

The solution proposed in this paper for determining the moment factors k_1 and k_2 was compared with the simplified formulations presented in [3] and [9], after being adapted to the assumptions used in those classical studies – namely, the symmetry of the material properties and the joint geometry – which reduces to $k_1 = k_2 = k$, thereby ensuring a proper basis for comparison (see Fig. 8):

$$k_1 = k_2 = k = \frac{1}{1+4\tanh\left(\frac{\lambda c}{4}\right)}, \qquad (39)$$

where k depends on a certain parameter λ [3, 9] and $c = \frac{1}{2}l$.
The results of these comparisons are presented in Fig. 8. The original solution developed by the authors, given by Eqs. (35) and (36) and further simplified in Eq. (39), falls within the expected range established by other researchers [3, 9].

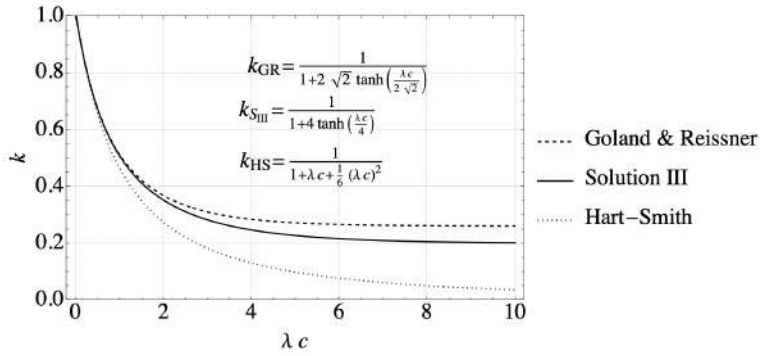

Figure 8: Plot of the moment factor k versus the product of λ and c, compared with the proposals formulated by Goland & Reissner [3] and Hart-Smith [9].

At this point, it should be emphasized once again that Eqs. (28)-(29) and the relations leading to Eqs. (31)-(38) were derived under the assumption that, in the central part of the joint, the cross-section behaves as a composite beam. Under this assumption, normal strains due to bending dominate over the relative slip between the layers, and the cross-sections remain approximately plane. This does not imply perfectly rigid bonding but rather a state in which the shear compliance of the adhesive layer mainly affects the stress and moment distributions in the transition zones, while the global bending stiffness can be represented by an effective cross-sectional stiffness.

The applicability range of this approximation depends on the relationship between the shear stiffness of the adhesive layer and the bending stiffness of the adherends. This relationship can be expressed using the dimensionless parameter

$$\eta = l \left(\frac{K_s}{D_b} \right)^{1/4}, \tag{40}$$

where $K_s \approx \dfrac{\overline{G}_3 b}{t_3}$ is the shear stiffness of the adhesive layer per unit length of the joint. The quantity $D_b = D_1 + D_2$ denotes the combined bending stiffness of the adherends.

The magnitude of η provides a direct interpretation of the degree of mechanical interaction between the adherends. For $\eta \gg 1$, the shear stiffness of the adhesive layer is large compared to the bending stiffness of the adherends over the characteristic length l. In this case, the relative slip between the adherends is small, the cross-sections remain approximately plane, and the joint behaves close to a mono-

lithic, fully composite beam. The effective bending stiffness and the associated bending moments predicted by the present model provide an accurate description of the global structural response. For $\eta \approx 1$, shear deformation in the adhesive layer becomes significant. Partial interaction between the adherends occurs, leading to noticeable but still moderate deviations from ideal composite-beam behavior. The proposed model remains applicable, however, larger differences may appear locally, especially near the ends of the bonded region where shear stresses and slip gradients are highest. For $\eta \ll 1$, the adhesive layer is relatively compliant in shear and the adherends tend to bend more independently. The composite-beam assumption then loses accuracy, and the global bending stiffness predicted by the model may be overestimated. In this regime, models that explicitly account for large interfacial slip and shear deformation along the entire overlap length are more appropriate. These effects can also be analyzed using FEM (see the Numerical examples section).

The next step in the analysis is to determine the stress state of the joint. According to classical beam-plate theory, the longitudinal normal stress $\sigma_{1x}(x, z_1)$ in the upper adherend of the joint is assumed to have the following form:

$$\sigma_{1x}(x, z_1) = \sigma_1^*(x) + \sigma_{1p}^*(x)\frac{z_1}{t_1}, \tag{41}$$

where the functions $\sigma_1^*(x)$ and $\sigma_{1p}^*(x)$ are unknowns that satisfy the following boundary conditions:

$$\begin{aligned}
&\sigma_1^*(x=0) = \frac{P}{bt_1},\\
&\sigma_{1p}^*(x=0) = -\frac{6k_1P}{bt_1},\\
&\sigma_1^*(x=l) = 0,\\
&\sigma_{1p}^*(x=l) = 0,\\
&\sigma_1^{*\prime}(x=0) = 0,\\
&\sigma_{1p}^{*\,\prime}(x=0) = -\frac{6P(-t_1 + k_1t_1 - t_2 + k_2t_2)}{blt_1^2},\\
&\sigma_1^{*\prime}(x=l) = 0,\\
&\sigma_{1p}^{*\,\prime}(x=l) = 0.
\end{aligned} \tag{42}$$

The assumed form of the function $\sigma_{1x}(x, z_1)$ in (41) and the boundary conditions given in (42) are based on the assumed distributions of normal and shear stresses illustrated in Fig. 9. At this point, it should be noted that Fig. 9 illustrates schematic

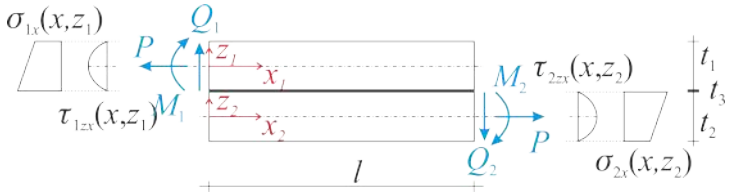

Figure 9: Assumed normal and shear stress distributions in the upper and lower adherend.

beam-level distributions of normal and shear stresses within the adherends resulting from the adopted kinematic and equilibrium assumptions. The shown shear stress distributions across the thickness of the adherends correspond to classical beam theory and are derived independently from the internal shear forces and bending moments, with zero values at the free surfaces. The apparent vanishing of shear stresses at the adhesive boundary should therefore not be interpreted as a representation of the actual interfacial shear stresses transmitted by the adhesive layer. In the analysis the load transfer between the bonded rods is accounted for implicitly through the equilibrium of the bonded system and the imposed compatibility conditions, rather than through an explicit resolution of the local three-dimensional stress field in the adhesive. A realistic description of nonzero interfacial shear stresses would require a refined layered or three-dimensional model explicitly incorporating the adhesive layer, which is beyond the scope of the present study focused on the global bending behavior.

Similarly, for the lower adherend, one obtains:

$$\sigma_{2x}(x, z_2) = \sigma_2^*(x) + \sigma_{2p}^*(x)\frac{z_2}{t_2}. \tag{43}$$

The corresponding boundary conditions are:

$$
\begin{aligned}
&\sigma_2^*(x=l) = \frac{P}{bt_2},\\
&\sigma_{2p}^*(x=l) = \frac{6k_2P}{bt_2},\\
&\sigma_2^*(x=0) = 0,\\
&\sigma_{2p}^*(x=0) = 0,\\
&\sigma_2^{*\prime}(x=l) = 0,\\
&\sigma_{2p}^{*\ \prime}(x=l) = \frac{6P(-t_1+k_1t_1-t_2+k_2t_2)}{blt_2^2},\\
&\sigma_2^{*\prime}(x=0) = 0,\\
&\sigma_{2p}^{*\ \prime}(x=0) = 0.
\end{aligned}
\tag{44}
$$

The conditions requiring the longitudinal derivatives of the stresses at the ends of the bonded region to be zero in Eqs. (42) and (44) follow directly from the assumed form of the stress distributions along the connection length. The stresses are approximated by smooth functions of the longitudinal coordinate x, derived from beam-level equilibrium relations and expressed in terms of internal forces and moments that vary continuously along the beam. Since no concentrated loads or singularities are applied at the ends of the bonded region, the stress fields must remain smooth there, which implies vanishing longitudinal stress gradients. The conditions imposed on the stress derivatives therefore ensure a regular, non-singular behavior of the assumed stress functions at the boundaries of the connection and are necessary for the consistency of the adopted beam-theoretical approximation. Next, by assuming equilibrium between the normal and shear stresses in adherend the following equilibrium equation applies:

$$
\frac{\partial \sigma_{ix}(x)}{\partial x} + \frac{\partial \tau_{izx}(x,z_i)}{\partial z_i} = 0, \tag{45}
$$

where $i = 1, 2$ (see Fig. 7). A function describing the shear stress in the upper adherend, $\tau_{1zx}(x, z_1)$, along the length of the joint can be determined by applying an additional boundary condition of the form $\tau_{1zx}(x, z_1 = \frac{t_1}{2}) = 0$. The resulting expression is:

$$
\tau_{1zx}(x,z_1) = \left(\frac{t_1}{2} - z_1\right)\sigma_1^*(x) + \left(\frac{t_1}{8} - \frac{z_1^2}{2t_1}\right)\sigma_{1p}^*(x). \tag{46}
$$

Applying the same procedure, but with the boundary condition $\tau_{2zx}(x, z_2 = -\frac{t_2}{2}) = 0$, the shear stress function in the lower adherend can be determined. The resulting expression is:

$$\tau_{2zx}(x, z_2) = \left(-\frac{t_2}{2} - z_2\right)\sigma_2^*(x) + \left(\frac{t_2}{8} - \frac{z_2^2}{2t_2}\right)\sigma_{2p}^*(x). \tag{47}$$

With the stress distributions $\tau_{izx}(x, z_i)$ now determined, equilibrium between the shear and normal stresses can be expressed as follows:

$$\frac{\partial \tau_{izx}(x, z_i)}{\partial x} + \frac{\partial \sigma_{ix}(x, z_i)}{\partial z_i} = 0. \tag{48}$$

For the upper adherend, applying the boundary condition $\sigma_{1x}(x, z_1 = \frac{t_1}{2}) = 0$, the normal stress in the z direction is given by:

$$\sigma_{1x}(x, z_1) = \left(\frac{t_1^2}{8} - \frac{t_1 z_1}{2} + \frac{z_1^2}{2}\right)\sigma_1^{*\prime\prime}(x) + \left(\frac{t_1^2}{24} - \frac{t_1 z_1}{8} + \frac{z_1^3}{6t_1}\right)\sigma_{1p}^{*\,\prime\prime}(x). \tag{49}$$

Similarly, for the lower adherend, by applying the boundary condition $\sigma_{2x}(x, z_2 = -\frac{t_2}{2}) = 0$, the following expression is obtained:

$$\sigma_{2x}(x, z_2) = \left(\frac{t_2^2}{8} + \frac{t_2 z_2}{2} + \frac{z_2^2}{2}\right)\sigma_2^{*\prime\prime} + \left(-\frac{t_2^2}{24} - \frac{t_2 z_2}{8} + \frac{z_2^3}{6t_2}\right)\sigma_{2p}^{*\,\prime\prime}. \tag{50}$$

Thus, the expression for the shear stress in the adhesive can be obtained either from (46) for the upper adherend at $z_1 = -\frac{t_1}{2}$, or from (47) for the lower adherend at $z_2 = \frac{t_2}{2}$, and is given by:

$$\tau_{3zx}(x) = t_1\sigma_1^{*\prime}(x) = -t_2\sigma_2^{*\prime}(x). \tag{51}$$

Next, the function describing the peel stress in the adhesive can be obtained from Eq. (49) for $z_1 = -\frac{t_1}{2}$ as follows:

$$\sigma_{3z}(x) = \frac{t_1^2}{2}\sigma_1^{*\prime\prime}(x) + \frac{t_1^2}{12}\sigma_{1p}^{*\,\prime\prime}(x). \tag{52}$$

Of course, the peel stress in the adhesive can also be determined from Eq. (50) for the lower adherend at $z_2 = \frac{t_2}{2}$.

At this stage, it remains to formulate a system of differential equations to determine the basis functions, such as $\sigma_1^*(x)$ and $\sigma_{1p}^*(x)$ for the upper adherend, using the previously described energy equation (27). However, to accomplish this, it is necessary to express all components describing the elastic strain energy of the individual layers (V_{10}, V_{20}, and V_{30}) solely in terms of the functions $\sigma_1^*(x)$ and $\sigma_{1p}^*(x)$. To obtain $V_{10}[\sigma_1^*(x), \sigma_{1p}^*(x)]$ and $V_{30}[\sigma_1^*(x), \sigma_{1p}^*(x)]$, it is sufficient to reorganize the previously derived functions (53), (58), (61), and (63). However, to determine $V_{20}[\sigma_1^*(x), \sigma_{1p}^*(x)]$, it is also necessary to apply additional equilibrium conditions (see Fig. 7), given as follows:

$$t_1\sigma_1^*(x) + t_2\sigma_2^*(x) = \frac{P}{b}, \tag{53}$$

$$t_3\ \tau_{3zx}(x) + \sigma_{2x}(x, z_2 = \frac{t_2}{2}) - \sigma_{1x}(x, z_1 = -\frac{t_1}{2}) = 0, \tag{54}$$

to determine the following functions:

$$\begin{aligned}\sigma_{2x}(x, z_2) = &\left(-\frac{t_1}{t_2} - \frac{6\,t_1^2 z_2}{t_2^3} - \frac{6\,t_1 z_2}{t_2^2} + \frac{12\,t_1 t_3 z_2}{t_2^3}\right)\sigma_1^*(x) + ... \\ &+\left(-\frac{t_1^2 z_2}{t_2^3}\right)\sigma_{1p}^*(x) + \frac{P\left[t_2^2 + 6(t_1 - k_1 t_1 + t_2 - 2t_3)z_2\right]}{bt_2^3} + ... \\ &+\frac{6P\left[(k_1-1)t_1 + (k_2-1)t_2 + 2t_3\right]xz_2}{blt_2^3},\end{aligned} \tag{55}$$

$$\begin{aligned}\tau_{2zx}(x, z_2) = &\left(-\frac{t_1}{4} - \frac{3t_1^2}{4t_2} + \frac{3t_1 t_3}{2t_2} + \frac{t_1 z_2}{t_2} + \frac{3t_1^2 z_2^2}{t_2^3} + \frac{3t_1 z_2^2}{t_2^2} - \frac{6t_1 t_3 z_2^2}{t_2^3}\right)\sigma_1^{*\prime}(x) + ... \\ &+\left(-\frac{t_1^2}{8t_2} + \frac{t_1^2 z_2^2}{2t_2^3}\right)\sigma_{1p}^{*\prime}(x) + ... \\ &+\frac{3P\left[(k_1-1)t_1 + (k_2-1)t_2 + 2t_3\right](t_2^2 - 4z_2^2)}{4blt_2^3},\end{aligned} \tag{56}$$

$$\sigma_{2x}(x,z_2)=\left(\frac{t_1^2}{4}+\frac{t_1t_2}{8}-\frac{t_1t_3}{2}+\frac{t_1z_2}{4}+\frac{3t_1^2z_2}{4t_2}-\frac{3t_1t_3z_2}{2t_2}+...\right.$$
$$\left.-\frac{t_1z_2^2}{2t_2}-\frac{t_1^2z_2^3}{t_2^3}-\frac{t_1z_2^3}{t_2^2}+\frac{2t_1t_3z_2^3}{t_2^3}\right)\sigma_1^{*\prime\prime}(x)+... \tag{57}$$
$$+\left(\frac{t_1^2}{24}+\frac{t_1^2z_2}{8t_2}-\frac{t_1^2z_2^3}{6t_2^3}\right)\sigma_{1p}^{*\ \prime\prime}(x).$$

The final forms of the expressions for V_{10}, V_{20}, and V_{30} are provided in the Digital appendix due to their complexity (https://drive.pg.edu.pl/s/bUwBtzGuG3BqnDk). Subsequently, by applying the principle of stationary potential energy and the methods of variational calculus, a system of Euler-Lagrange differential equations is derived:

$$\begin{cases} a_1+a_2x+a_3\sigma_1^*(x)+a_4\sigma_{1p}^*(x)+a_5\sigma_1^{*\prime\prime}(x)+a_6\sigma_{1p}^{*\ \prime\prime}(x)+... \\ \quad +a_7\sigma_1^{*\prime\prime\prime\prime}(x)+a_8\sigma_{1p}^{*\ \prime\prime\prime\prime}(x)=0, \\ a_9+a_{10}x+a_{11}\sigma_1^*(x)+a_{12}\sigma_{1p}^*(x)+a_{13}\sigma_1^{*\prime\prime}(x)+a_{14}\sigma_{1p}^{*\ \prime\prime}(x)+... \\ \quad +a_{15}\sigma_1^{*\prime\prime\prime\prime}(x)+a_{16}\sigma_{1p}^{*\ \prime\prime\prime\prime}(x)=0, \end{cases} \tag{58}$$

where, for the first and second equations, the coefficients a_1 to a_{16} are listed in the appendix at the end of the paper (see 75 and 76).

In order to obtain an analytical solution to the system of differential equations (58), it is necessary to apply the superposition of the homogeneous ($\sigma_{1h}^*(x)$, $\sigma_{1ph}^*(x)$) and particular ($\sigma_{1s}^*(x)$, $\sigma_{1ps}^*(x)$) solutions.

First, attention should be given to the particular solution, under the assumption that:

$$\begin{aligned} \sigma_{1s}^*(x)&=H_0x+H_1, \\ \sigma_{1ps}^*(x)&=I_0x+I_1, \end{aligned} \tag{59}$$

and by solving a system of equations of the following form:

$$\begin{cases} a_1+a_3H_1+a_4I_1+(a_2+a_3H_0+a_4I_0)x=0, \\ a_9+a_{11}H_1+a_{12}I_1+(a_{10}+a_{11}H_0+a_{12}I_0)x=0, \end{cases} \tag{60}$$

first with respect to H_0 and I_0:

$$\begin{cases} a_2 + a_3 H_0 + a_4 I_0 = 0, \\ a_{10} + a_{11} H_0 + a_{12} I_0 = 0, \end{cases} \tag{61}$$

where $H_0 = \frac{a_{12}a_2 - a_{10}a_4}{a_{11}a_4 - a_{12}a_3}$ and $I_0 = \frac{a_{11}a_2 - a_{10}a_3}{a_{12}a_3 - a_{11}a_4}$, and then with respect to H_1 and I_1:

$$\begin{cases} a_1 + a_3 H_1 + a_4 I_1 = 0, \\ a_9 + a_{11} H_1 + a_{12} I_1 = 0, \end{cases} \tag{62}$$

where $H_1 = \frac{a_1 a_{12} - a_4 a_9}{a_{11}a_4 - a_{12}a_3}$ and $I_1 = \frac{a_1 a_{11} - a_3 a_9}{a_{12}a_3 - a_{11}a_4}$.

From this, the particular part of the solution is given by:

$$\begin{aligned} \sigma_{1s}^*(x) &= \frac{a_{12}a_2 - a_{10}a_4}{a_{11}a_4 - a_{12}a_3} x + \frac{a_1 a_{12} - a_4 a_9}{a_{11}a_4 - a_{12}a_3}, \\ \sigma_{1ps}^*(x) &= \frac{a_{11}a_2 - a_{10}a_3}{a_{12}a_3 - a_{11}a_4} x + \frac{a_1 a_{11} - a_3 a_9}{a_{12}a_3 - a_{11}a_4}. \end{aligned} \tag{63}$$

Second, the solution to the homogeneous system is sought under the following assumption:

$$\begin{aligned} \sigma_{1h}^*(x) &= C_1 e^{\lambda_1 x} + C_2 e^{-\lambda_1 x} + C_3 e^{\lambda_2 x} + C_4 e^{-\lambda_2 x}, \\ \sigma_{1ph}^*(x) &= C_5 e^{\lambda_3 x} + C_6 e^{-\lambda_3 x} + C_7 e^{\lambda_4 x} + C_8 e^{-\lambda_4 x}, \end{aligned} \tag{64}$$

by specifying the values of $\lambda_1 = \frac{\sqrt{-\left(\frac{a_5}{a_7}\right) + \frac{\sqrt{a_5^2 - 4a_3a_7}}{a_7}}}{\sqrt{2}}$, $\lambda_2 = \frac{\sqrt{-\left(\frac{a_{13}}{a_{15}}\right) + \frac{\sqrt{a_{13}^2 - 4a_{11}a_{15}}}{a_{15}}}}{\sqrt{2}}$, $\lambda_3 = \frac{\sqrt{-\left(\frac{a_6}{a_8}\right) - \frac{\sqrt{a_6^2 - 4a_4a_8}}{a_8}}}{\sqrt{2}}$, and $\lambda_4 = \frac{\sqrt{-\left(\frac{a_{14}}{a_{16}}\right) + \frac{\sqrt{a_{14}^2 - 4a_{12}a_{16}}}{a_{16}}}}{\sqrt{2}}$. The values of λ_i at i=1, 2, 3, 4 are determined by solving the characteristic equations, which are algebraic equations obtained by substituting the exponential solution (64) into the differential equation (58). Next, the constants C_1 to C_8 are determined using the boundary conditions given in (42). The expressions for the constants C_1 to C_8, which result from these assumptions, are provided in the Digital appendix due to their complexity (https://drive.pg.edu.pl/s/bUwBtzGuG3BqnDk).

Ultimately, the functions $\sigma_1^*(x)$ and $\sigma_{1p}^*(x)$ take the form of the sum of Eqs. (64) and (63):

$$\begin{aligned} \sigma_1^*(x) &= \sigma_{1h}^*(x) + \sigma_{1s}^*(x), \\ \sigma_{1p}^*(x) &= \sigma_{1ph}^*(x) + \sigma_{1ps}^*(x). \end{aligned} \tag{65}$$

Substituting the function from Eq. (65) into Eqs. (51) and (52) yields the desired shear and normal stress distribution functions at the interface between the adhesive and the bottom plate.

At this point, it should be emphasized that the proposed solution is subject to the limitations inherent to Euler-Bernoulli beam theory. In particular, transverse shear deformations in the adherends are neglected and plane sections are assumed to remain plane, which restricts the model to relatively slender elements. It should also be noted that the adhesive layer is assumed to be thin and linearly elastic and therefore, thickness-wise stress gradients, material nonlinearity, and damage effects are not explicitly taken into account. The limitations on the adhesive thickness t_3 arising from the assumptions of the proposed model can be formulated as follows:

$$\frac{\alpha_p^2 l^2 G_3}{tE} \leq t_3 \leq \eta_p t \qquad \text{and} \qquad t/l << 1, \tag{66}$$

where α_p is a dimensionless parameter related to the characteristic decay rate of shear stresses in the overlap, governing the extent of the edge-effect zone (typically $\alpha_p = 0.05 - 0.1$), η_p is a dimensionless upper-bound parameter defining the admissible ratio between the adhesive thickness and the adherend thickness, consistent with the thin-layer assumption (typically $\eta_p = 0.02 - 0.05$), E is the Young's modulus of the adherend material, t is the thickness of a single adherend, and l denotes the joint overlap length. It should be emphasized that the parameters α_p and η_p are not material constants but model parameters defining the admissible asymptotic range of the beam-layer idealization. The parameter α_p controls the relative extent of the edge-effect zone with respect to the overlap length and is assumed to be of the order of a few percent, which ensures that the boundary layer remains localized and mechanically distinguishable from the regular overlap region. The parameter η_p defines the maximum admissible ratio between the adhesive thickness and the adherend thickness, preserving the thin-layer assumption and ensuring mechanical consistency of the beam model, in which the global response is governed primarily by bending of the adherends, while the adhesive layer provides compatible shear transfer between them. The proposed ranges should therefore be interpreted as engineering order-of-magnitude estimates rather than strict thresholds. Furthermore, the formulation eq. (66) also assumes slender adherends, meaning that the adherend thickness t remains much smaller than the overlap length l. In engineering practice this typically corresponds to thickness-to-overlap ratios in the range of about 0.01-0.1, while a more restrictive interpretation consistent with the Euler-Bernoulli beam assumption is below approximately 0.05.

The two-sided limitation on the adhesive layer thickness eq. (66) defines a physically justified "operating window" of the beam–layer model, within which two conditions are simultaneously satisfied: an accurate description of the global joint response and a non-degenerate distribution of shear stresses along the overlap. The upper bound $t_3 \leq \eta_p t$ ensures that the adhesive behaves as a thin interlayer relative to the adherend thickness. This preserves the mechanical consistency of the beam idealization and guarantees that the global response remains governed primarily by bending of the adherends, while the adhesive layer provides shear transfer between them. The lower bound $t_3 \geq \alpha_p^2 l^2 G_3/(tE)$ ensures that the characteristic load-transfer length remains sufficiently large for edge effects to be physically meaningful and for the shear stress distribution to avoid degeneration into an almost uniform profile.

Within the specified range, the model remains mechanically consistent, preserves the interpretability of its parameters, and enables the simultaneous capture of the global joint response and physically meaningful edge effects.

Numerical examples corresponding to Solutions III are presented in the Figs. 16, 17, and 18 in section Numerical examples.

3. Theoretical validation

First, the proposed analytical solution for Case III was validated by comparing it with the solutions of Goland & Reissner [3] and Hart-Smith [9]. The simplified solution developed by Goland & Reissner was adapted to the coordinate system adopted in this paper, in which the longitudinal coordinate is measured from the edge of the joint rather than from its center. It should be emphasized that the original Goland & Reissner solution assumes symmetry with respect to the center of the joint, which is why the corresponding formulations and illustrations are typically presented only for the region extending from the edge to the center. The Goland & Reissner solution, rewritten in the adopted coordinate system, is summarized in Eqs. (67–69). The following relations describe the relevant normal and shear stress components in a single-lap adhesive joint according to the Goland & Reissner model. The term $\sigma_{1GR}(x)$ denotes the normal stresses developing in the upper adherend as a result of the applied tensile load. The quantity $\sigma_{3GR}(x)$ corresponds to the peel stresses acting in the adhesive layer, i.e., normal tensile stresses perpendicular to the bond line. In turn, $\tau_{3GR}(x)$ denotes the shear stresses in the adhesive, transferred parallel to the bonded interface. The expressions in Eqs. (67–69) are represented as infinite series over the integer index n, where $n = 1, 2, 3, \ldots$. The index n corresponds to successive modes of the analytical solution arising from

the eigenvalue problem associated with the Goland & Reissner formulation. Each term contributes a modal component to the stress field, characterized by an exponential spatial variation and a weighting factor determined by the corresponding eigenvalue α_n. The complete stress field is obtained as a superposition of these modal contributions. In practical computations, the infinite series is approximated by truncating it to a finite number of terms N. The truncation parameter N is selected using a tail - convergence test applied to partial sums evaluated on a spatial grid that is densified near the boundaries of the interval. For each candidate value of N, the series is computed using N, $2N$, and optionally $4N$ terms. The tail error is estimated as the maximum absolute difference between successive partial sums over the grid, i.e. $\max\left(|S_{2N}(x) - S_N(x)|,\ |S_{4N}(x) - S_{2N}(x)|\right)$. The parameter N is doubled iteratively until this error falls below a prescribed tolerance, or until a prescribed upper limit $N_{\max}$ is reached. Different spatial ranges are used depending on the symmetry properties of the solution. Details of the procedure can be found in the Digital appendix (https://drive.pg.edu.pl/s/bUwBtzGuG3BqnDk).

$$\sigma_{1\mathrm{GR}}(x) = \frac{p}{2} + \sum_{n=1}^{\infty} C_n \left\{ \frac{1}{2} e^{\alpha_n (x-l)} [\alpha_n (l-x) + 1] \right\} \cos\left(\alpha_n \frac{t_1}{2}\right) \tag{67}$$

$$\tau_{3\mathrm{GR}}(x) = -\sum_{n=1}^{\infty} C_n \left\{ \frac{1}{2} e^{\alpha_n \left(|x-\frac{l}{2}|-\frac{l}{2}\right)} \alpha_n \left(\left| x - \frac{l}{2} \right| - \frac{l}{2} \right) \right\} \sin(\alpha_n t_1), \tag{68}$$

$$\sigma_{3\mathrm{GR}}(x) = \sum_{n=1}^{\infty} C_n \left\{ \frac{1}{2} e^{\alpha_n \left(|x-\frac{l}{2}|-\frac{l}{2}\right)} \left[\alpha_n \left(\left| x - \frac{l}{2} \right| - \frac{l}{2} \right) + 1 \right] \right\} \cos(\alpha_n t_1), \tag{69}$$

where

$$C_n = \frac{4p}{n\pi} \left\{ \frac{12 k_{GR}}{n\pi} \left[\cos\left(\frac{n\pi}{2}\right) - \cos(n\pi) \right] - (3k_{GR} + 1) \sin\left(\frac{n\pi}{2}\right) \right\},$$

and

$$p = \frac{P}{b\, t_1},\ k_{GR} = \frac{1}{1 + 2\sqrt{2} \tanh\left(\frac{l\, \lambda_{GR}}{4\sqrt{2}}\right)},\ \lambda_{GR} = \sqrt{12(1-\overline{\nu}_1^2)} \frac{\sqrt{\frac{p}{\overline{E}_1}}}{t_1},\ \alpha_n = \frac{n\pi}{2t_1}.$$

The solutions proposed by Hart-Smith are shown in Eqs. (70, 71). In contrast to the Goland & Reissner formulation, where the stress components are expressed as functions of the coordinate x, the Hart-Smith model provides closed-form expressions for the extreme stresses in the adhesive layer. The term τ_{3HS}^{max} denotes the

maximum shear stress that may develop in the adhesive joint, while σ_{3HS}^{max} corresponds to the maximum peel stress acting perpendicular to the bond line. These quantities define the critical stress levels that govern the onset of adhesive failure and are therefore of particular importance in the strength assessment and design of bonded joints.

$$\tau_{3HS}^{\max} = \tau_{av}\left\{1 + \frac{\lambda_{HS}^2}{4\lambda_p^2}\left[1 + \frac{3k_{HS}(1-\overline{\nu}_1^2)}{k_b}\left(1 + \frac{t_3}{t_1}\right)\right]\left[\frac{l\lambda_p}{\tanh(l\lambda_p)} - 1\right]\right\}, \quad (70)$$

$$\sigma_{3HS}^{\max} = \frac{\overline{E}_3 k_{HS} P t_1}{4 t_3 D_1 \chi^2}\left(1 + \frac{t_3}{t_1}\right), \quad (71)$$

where

$$\tau_{av} = -\frac{P}{bl},\ \lambda_{HS} = \sqrt{\frac{2\overline{G}_3}{\overline{E}_1 t_1 t_3}},\ \lambda_p = \sqrt{\frac{\lambda_{HS}^2}{4}\left[1 + \frac{3(1-\overline{\nu}^2)}{k_b}\right]},$$

$$k_{HS} = \frac{1}{1 + \frac{l\lambda_{HS}}{2} + \frac{1}{6}\left(\frac{l\lambda_{HS}}{2}\right)^2},\ k_b = D_1\frac{12(1-\overline{\nu}_1^2)}{\overline{E}_1 t_1^3},$$

$$\overline{G}_3 = \frac{\overline{E}_3}{2(1+\overline{\nu}_3)},\ D_1 = \frac{1}{12}\overline{E}_1 b t_1^3,\ \chi = \sqrt[4]{\frac{\overline{E}_3}{2t_3 D_1}}.$$

4. FEM validation

Secondly, FE models were developed to validate the proposed analytical solutions. The simulations were carried out using the Abaqus software. The model represents a three-dimensional single-lap adhesive joint, and its static scheme is shown in Fig. 10. To reduce computational cost, only half of the joint was modeled by introducing a symmetry plane along its longitudinal mid-plane. The model was discretized using C3D8R elements, i.e., eight-node linear brick elements with reduced integration and hourglass control. A graded mesh density was applied to accurately capture stress gradients within the adhesive layer and in the adjacent adherend regions. In the adhesive layer ($t_3 = 0.05$ mm), the element dimensions were approximately 0.0125/0.025/0.1 mm; in the adherend region adjacent to the adhesive, 0.025/0.025/0.1 mm; and in the outer adherend regions, 0.2/0.2/0.1 mm. The total number of elements for overlap lengths of 12.5 mm, 25.0 mm, and 37.5 mm was approximately 3.36×10^6, 6.36×10^6, and 9.90×10^6,

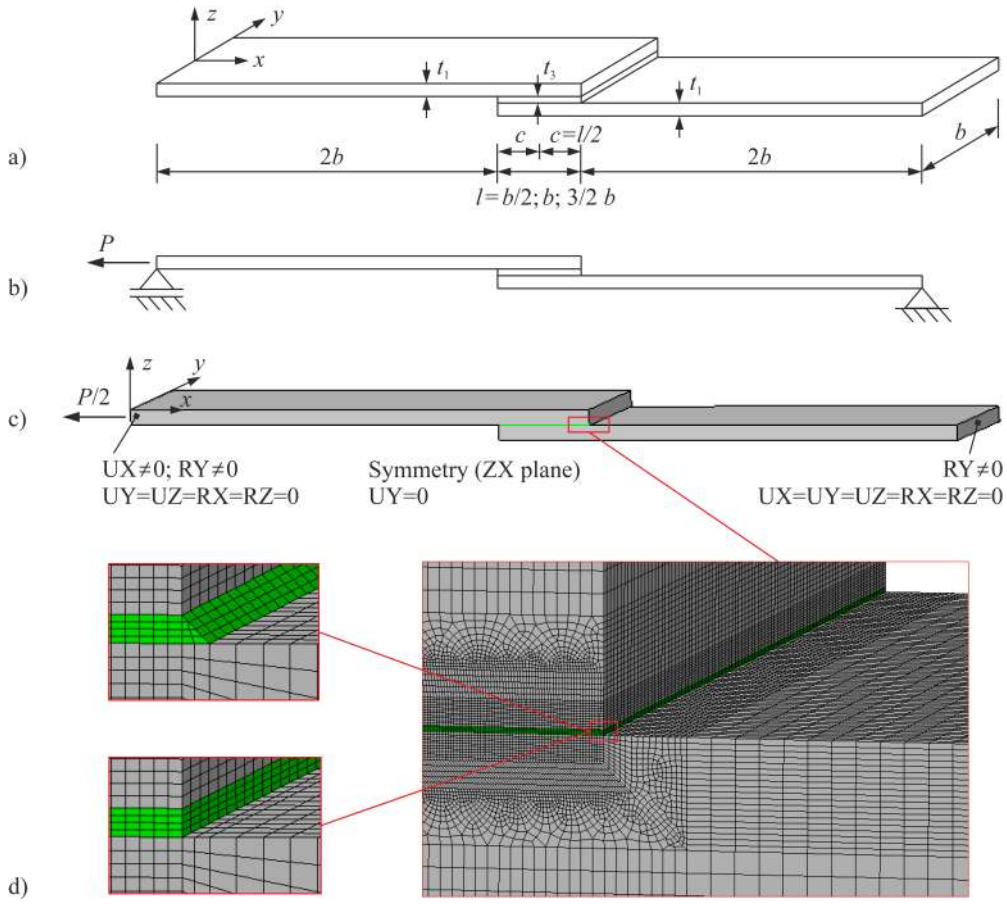

Figure 10: FEM model of the single-lap joint: a) geometry, b) static scheme, c) boundary conditions, and d) FEM mesh

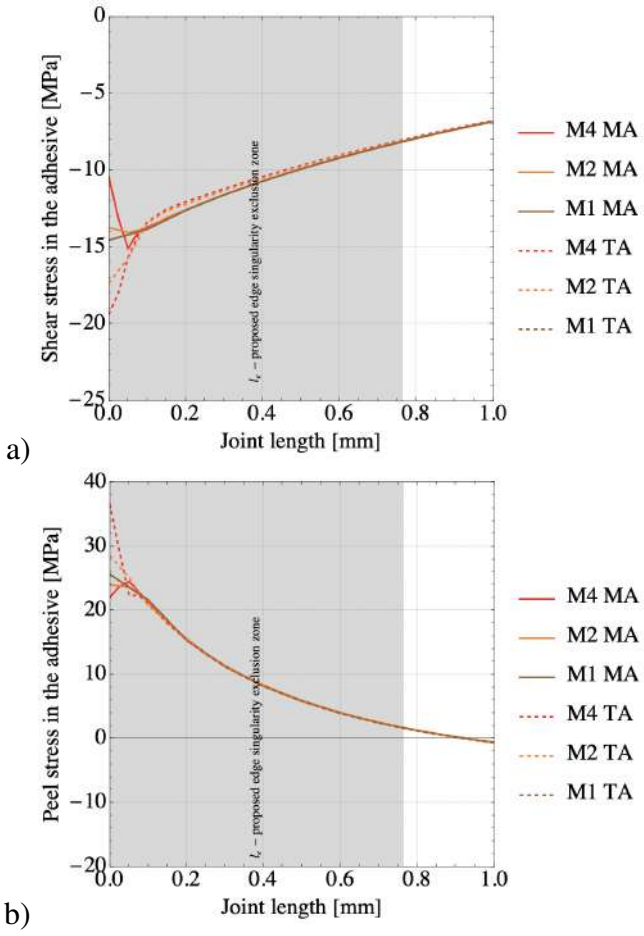

Figure 11: Shear and peel stress distributions in the adhesive mid-layer (MA) and the top layer at the adherend interface (TA) near the overlap edge for the FEML model with different mesh densities for $l = 25$ mm, highlighting mesh-dependent edge effects associated with the singular stress field: a) shear, b) peel (M4 – 4 elements, M2 – 2 elements, M1 – 1 element through the adhesive thickness)

respectively. Such a high mesh density was necessary to obtain accurate stress distributions in the critical regions of the joint. The boundary conditions were defined by kinematically coupling the end surfaces of both adherends to reference points, at which pinned supports were applied. The load was introduced as a concentrated tensile force acting along the longitudinal axis of the joint at the reference point of the left adherend. Two main types of FEM models were developed: linear and nonlinear. In the linear models, both adherends and the adhesive were assumed to be linearly elastic and isotropic. These models differed in the representation of the adhesive edges: the basic model neglected adhesive spew fillets (FEML), whereas the improved model explicitly included them (FEMLS). The nonlinear models incorporated material nonlinearity (FEMMNS), geometric nonlinearity (FEMGNS), and their combined effect (FEMGMNS), with material properties determined from the authors' experimental studies [49, 38]. Models including adhesive fillets were analyzed only for a single overlap length, $l = 25$ mm. A key issue in the FE analysis arises from the significant mismatch in elastic properties between the aluminum adherends and the adhesive layer, with the Young's modulus ratio $E_{1,2}/E_3 \approx 39$. This leads to the classical bi-material singularity at the interface edge, where the stress field follows a power-law form $\sigma \sim r^{\lambda_D - 1}$. For the considered material parameters ($\nu_1 = \nu_2 = 0.37$, $\nu_3 = 0.33$), the Dundurs parameters are $\alpha \approx 0.94$ and $\beta \approx 0.30$ (plane stress) or 0.19 (plane strain), corresponding to $\lambda_D \approx 0.64$ and $\lambda_D \approx 0.62$, respectively. Consequently, the stress behaves as $\sigma \sim r^{-0.37}$, which implies a strong, non-integrable singularity at the interface corner. This singularity is further intensified by the presence of right-angle corners between dissimilar materials. As a result, the stress field in the immediate vicinity of the overlap edge is governed by the singular solution and does not represent physically meaningful structural stresses. In practice, this manifests as a lack of convergence of peak stresses under mesh refinement, which is a characteristic feature of a mathematical singularity rather than a numerical error. Therefore, further mesh refinement at the overlap edges does not improve solution accuracy. Due to the singularity near the overlap edge, both the stress magnitude and the exact location of extreme values are inherently ambiguous and method-dependent [32, 50]. To obtain physically meaningful results, stresses were evaluated at a finite distance from the overlap edge rather than directly at the interface. In the present study, a reference distance in the form $l_e \sim \sqrt[4]{t^3\, t_3}$ was adopted, reflecting the geometric scaling. For the considered joint parameters, this yields $l_e \approx 0.765$ mm (approximately $15\, t_3$). It should be noted that the value of l_e also depends on the material mismatch between the adherends and the adhesive, which, together with geometric discontinuities, deter-

mines the extent of the bi-material singularity and the associated exclusion zone. Although the region of pronounced stress gradients observed in the FEM results may vary, it is generally confined to a finite distance from the edge - on the order of approximately 1% for shear stresses and decreasing to about 0.5% for peel stresses relative to the joint length (for $l = 25$ mm, i.e., approximately 0.7 mm for shear and 0.1 mm for peel, Fig. 11) - the influence of the singular stress field can be conservatively described by the proposed parameter l_e. Accordingly, a more conservative reference distance was adopted to ensure that the evaluated stresses are governed primarily by global load transfer rather than by local edge effects. The introduction of a finite evaluation distance is a standard approach in the presence of interface singularities and allows for a physically meaningful comparison between analytical and numerical results. To assess the influence of geometric modifications, an improved model including adhesive fillets (FEMLS) was also analyzed. Although rounding the adhesive edges modifies the local geometry and may reduce the geometric singularity, its effect on the overall stress distribution remains limited. In the case of the thin adhesive layer considered here, the stress field is governed primarily by the stiffness mismatch between the adherends and the adhesive, while the local edge geometry plays a secondary, albeit non-negligible, role. It should also be noted that introducing geometric features such as fillets or chamfers effectively alters the boundary conditions and corresponds to a different structural configuration, in which the sharp bi-material corner is replaced by a finite-radius transition. Although such modifications may reduce local stress concentrations, their overall effect on the stress distribution remains limited and does not eliminate the singularity problem, particularly for thin adhesive layers. For this reason, the adopted methodology, based on the FEML model and the evaluation of stresses at a finite distance from the edge ($\sim l_e$), is well justified. Finally, nonlinear models (FEMGNS, FEMMNS, FEMGMNS) were employed to provide additional validation of the analytical solution (Solution III) in the nonlinear operating range of the joint, particularly in the vicinity of the lap edge. While the inclusion of material and geometric nonlinearities leads to a partial mitigation of singularity effects, it does not eliminate them, even at the center of the adhesive layer (see Fig. 19). The results of FEM analyses are presented in the Numerical Examples section.

5. Experimental validation

Thirdly, parallel experimental studies (Figs. 12, 13) were conducted to verify, as far as possible, the accuracy of the proposed analytical solution (Solution III). It should be emphasised that full experimental validation of the joint is not feasible

or would be extremely difficult to implement. Therefore, the experimental comparisons should be regarded as supplementary yet highly important evidence. The experimental programme constitutes a continuation of the authors' earlier studies [49, 38].

Single-lap joints were fabricated from aluminium alloy (6060-T6) adherends bonded with DP490 epoxy adhesive. Prior to bonding, the adherend surfaces were mechanically prepared using low-grit abrasive paper in order to increase surface roughness and promote mechanical interlocking. Subsequently, the surfaces were degreased to remove contaminants and ensure proper adhesion. The thickness of the adhesive layer was controlled in an indirect but repeatable manner through the application of a constant clamping force using a dedicated mechanical fixture. As a result of the constant pressure and fixed bonded area, the adhesive thickness stabilised within a narrow range, varying approximately between $t_3 = 0.04$ mm and 0.06 mm, with a nominal value of 0.05 mm assumed in the analytical and numerical models. This approach reflects typical engineering practice, where strict local control of adhesive thickness is difficult, and the resulting thickness should be interpreted as an effective parameter governing the global stiffness of the joint. As part of the experiment, the strain state in the loading direction was measured at selected external points: at the beginning of the overlap ($x = 0$, point 1) and at mid-length ($x = l/2$, point 2), on both sides of the joint. A total of nine specimens were tested, corresponding to three overlap lengths: $l = 12.5$ mm, 25.0 mm, and 37.5 mm. The tests were carried out using a Zwick Z100 universal testing machine under displacement control at a constant rate of 1 mm/min. The applied force was measured using a 5 kN load cell. Strains were recorded using electrical resistance strain gauges (HBM 1-LY43-0.6/120) connected to an HBM amplifier (1-MX840B). A strain gauge with a base length of 0.6 mm was selected as a pragmatic compromise between spatial resolution and measurement reliability (13a). On the one hand, a short gauge length is required to capture steep strain gradients, particularly near the overlap edge. On the other hand, excessively small gauges increase sensitivity to positioning errors and measurement noise. The adopted gauge length therefore represents a balanced engineering choice enabling consistent and repeatable measurements. It should be noted that the strain field near the overlap edge is highly non-uniform, with stress values decreasing rapidly over a short distance (on the order of a few millimetres). In addition, precise identification of the exact edge location introduces further uncertainty. Consequently, the measured values in this region should be interpreted as spatially averaged quantities rather than exact local extrema. This observation is consistent with the adopted analytical framework, in which stresses are interpreted as effective structural quanti-

ties, particularly in regions influenced by edge effects. This approach is consistent with the objective of the present study, which is not to resolve local singular stress fields at the overlap edge, but rather to provide a physically meaningful and structurally representative description of the global load transfer in the joint. In addition to the local strain measurements obtained using strain gauges, the global strain of the joints was evaluated independently using a clamp-on extensometer with a gauge length of $L_0 = 50$ mm. Due to geometric limitations and the placement of strain gauges, it was not possible to perform extensometer measurements on the same specimens. Therefore, the extensometer measurements were conducted on an additional set of nine samples of three specimens per each length of overlap with identical geometric and material parameters as the strain-gauge-instrumented joints. The extensometer provided an averaged strain response representative of the overall deformation of the joint, serving as a reference for the global structural behavior. Although the local and global measurements were not obtained from the same specimens, the adopted approach ensured consistency at the level of nominal response by maintaining identical testing conditions and specimen configurations. This enables a meaningful qualitative comparison between local strain measurements and the global deformation characteristics of the joint. Such supplementary global measurements are particularly important for bonded joints, where strong strain gradients occur, and local measurements alone may not fully capture the overall structural response.

Figure 13b shows an example specimen positioned in the grips of a universal testing machine. Additionally, transverse strains were observed at x=l (point 3). However, since this direction is not analyzed in the present study, these results are not included in the paper. The measurement results, obtained after converting the average strain values into stresses, are presented in Fig. 16 for points x=0 (point 1) and x=$l/2$ (point 2), for three different joint lengths: 12.5, 25.0, and 37.5 mm.

It should be emphasized that the experimental validation presented in this study is subject to inherent limitations associated with the use of strain gauges for strain and stress estimation. Strain gauges provide localized, spatially averaged measurements and are therefore not well suited for capturing the highly non-uniform strain fields that develop in adhesively bonded joints, particularly near the overlap edges where steep gradients and stress singularities occur. Consequently, the experimental results should be interpreted primarily as qualitative support for the analytical trends rather than as a full-field quantitative validation.

It is acknowledged that full-field optical measurement techniques based on Digital Image Correlation [51] can, in principle, provide more detailed information on strain distributions in bonded joints. However, due to the very small characteris-

tic dimensions of the investigated region - especially the adhesive layer thickness (0.05 mm) and the narrow zones of stress concentration - the application of conventional DIC is insufficient. A reliable experimental characterization would require the use of micro-scale Digital Image Correlation (micro-DIC), which allows strain measurements over very small fields of view with high spatial resolution.

Furthermore, the main FEML model used in the analysis was experimentally validated by comparing the predicted and measured load-elongation responses of single-lap joints over the loading range from 0 to 1 kN, as shown in Fig. 14. In accordance with standard validation procedures for bonded joints, the global load-elongation response was first examined in order to assess the consistency between the experimental measurements and the numerical model. The elongation was measured over a fixed gauge length of $L_0 = 50$ mm, while the numerical results were obtained from the FEML model. The validation was carried out for three overlap lengths, namely $l = 12.5$, 25, and 37.5 mm. The Pearson correlation coefficients calculated between the experimental and numerical load-elongation (P–Δ) curves over the full loading range are equal to 0.9990 for $l = 12.5$ mm, 0.9977 for $l = 25$ mm, and 0.9995 for $l = 37.5$ mm. These coefficients quantify the similarity in the shape of the global load-elongation response and should not be interpreted as a measure of agreement in local stress or strain fields. Thus, the high correlation values indicate that the FEML model correctly reproduces the overall trend of the structural response. However, they do not imply strict quantitative agreement in terms of the absolute elongation values. Indeed, visible differences can be observed between the experimental and FEM-predicted load-elongation curves, particularly at higher load levels, where the discrepancies in absolute elongation become more pronounced. For this reason, within the scope of the present study, the agreement between the experimental and numerical results should be interpreted as qualitative rather than strictly quantitative. These differences can be attributed to several factors, including (i) idealized boundary conditions in the FEM model, (ii) the simplified linear-elastic and averaged representation of the adhesive layer, and (iii) the neglect of local compliance effects and experimental uncertainties. In particular, the boundary conditions play a significant role. In the experiments, the specimen ends were effectively clamped in the testing grips, which introduced partial rotational restraint. In contrast, the FEM model employed idealized pinned supports. As a result, the experimental configuration exhibited higher effective stiffness, since clamping reduced the bending-induced deformations characteristic of single-lap joints, whereas the FEM model predicted a more compliant response. Additional differences may also arise from the inability of the FEML model to capture the nonlinear behavior and geometric imperfections of the adhesive.

Following the verification of the global load-elongation response, the validation was further extended to strain-gauge measurements, which provide additional insight into the local deformation behavior and confirm the consistency of the predicted trends along the overlap. Specifically, the experimentally measured strains were compared with the corresponding numerical predictions at selected locations, namely at the beginning ($x = 0$) and at the mid-length ($x = l/2$) of the overlap, for the three joint lengths considered. The results are presented in Fig. 15. A clear difference in the level of agreement between the FEML model and the experimental results is observed depending on the location within the overlap. At the overlap edge ($x = 0$), a significant scatter of the experimental data is present, with the measured strains ranging from compressive to slightly tensile values for $l = 12.5$ mm and approaching near-zero values for longer overlaps. In this region, the FEML model consistently predicts more compressive strains than the experimental average and lies close to the lower bound of the experimental range. In contrast, at the mid-length of the overlap ($x = l/2$), the agreement is very good, with minimal experimental scatter and FEML predictions closely matching the experimental values. This confirms that the model accurately captures the global load-transfer behavior in the central region of the joint. The pronounced scatter observed at the overlap edge should be attributed primarily to the presence of a singularity, which leads to strong localization of the stress and strain fields. In this region, both experimental measurements and numerical predictions are highly sensitive to the exact position and local geometry, which naturally results in significant variability. Therefore, the observed discrepancies at $x = 0$ do not indicate a deficiency of the FEML model, but rather reflect the inherent limitations in defining representative strain values at the joint edge. In contrast, the excellent agreement observed at the mid-length confirms that the model accurately captures the global load-transfer mechanisms governing the joint behavior.

6. Numerical examples

The numerical examples consider a single-lap joint (see Figs. 2 and 10) composed of two 6060-T6 aluminum-alloy adherends with a constant width (b=25 mm), bonded with a 3M™ Scotch-Weld™ DP490 epoxy adhesive. The 6060-T6 aluminum alloy has a modulus of elasticity of 66,867 MPa and a Poisson's ratio of 0.33 [38], while the DP490 adhesive is characterized by E_3=1715 MPa and ν_3=0.37 [49]. The joint was subjected to a tensile load of 1 kN. The only variable parameter in the numerical examples is the overlap length l (l=1/2b=12.5 mm, l=b=25.0 mm, l=3/2b=37.5 mm), while the adherend thicknesses (t_1=t_2=1.9 mm),

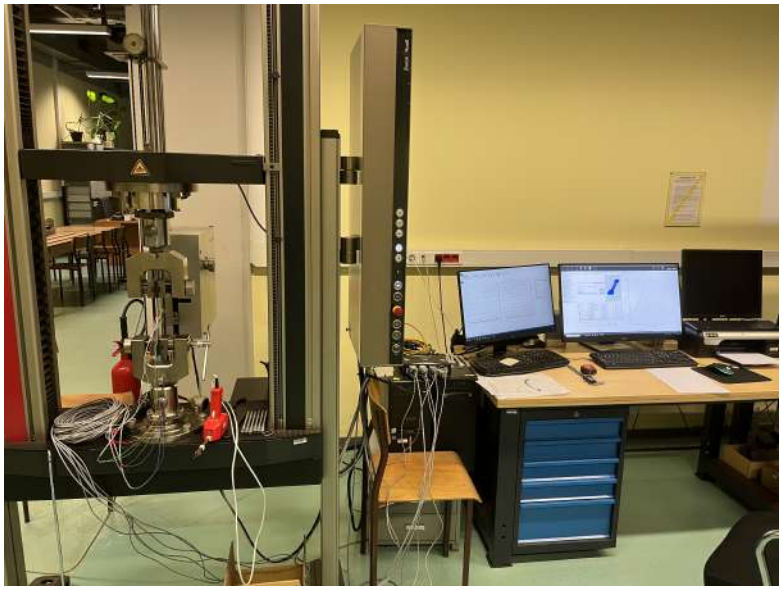

Figure 12: General view of the experimental test setup used for tensile testing with integrated strain-gauge data acquisition

the adhesive-layer thickness (t_3=0.05 mm), and the adherend extension lengths (l_1=l_2=50 mm) were kept constant. In the numerically analyzed cases, for l=12.5, 25.0, and 37.5 mm, the parameter η (see Eq. (66)), taking into account the remaining geometric and material variables, was equal to 7.7, 15.5, and 23.2, respectively. In all analyzed cases, η>1, which means that the conditions for the applicability of the proposed solution are satisfied.

Additionally, in order to quantitatively verify the assumption that the bonded structure behaves as a monolithic beam, a numerical analysis of interlayer slip was performed using the FEM. The objective of this analysis was to evaluate the degree of composite action between the load-carrying layers within the bonded overlap region.

The relative longitudinal slip between the layers was defined as

$$s(x) = u_1(x) - u_2(x), \tag{72}$$

where $u_1(x)$ and $u_2(x)$ denote the longitudinal displacements of points located at the interfaces between each load-carrying layer and the adhesive layer. For each configuration, the maximum absolute value of slip along the overlap length l was determined as

$$s_{\max} = \max_{x\in[0,l]} |s(x)|. \tag{73}$$

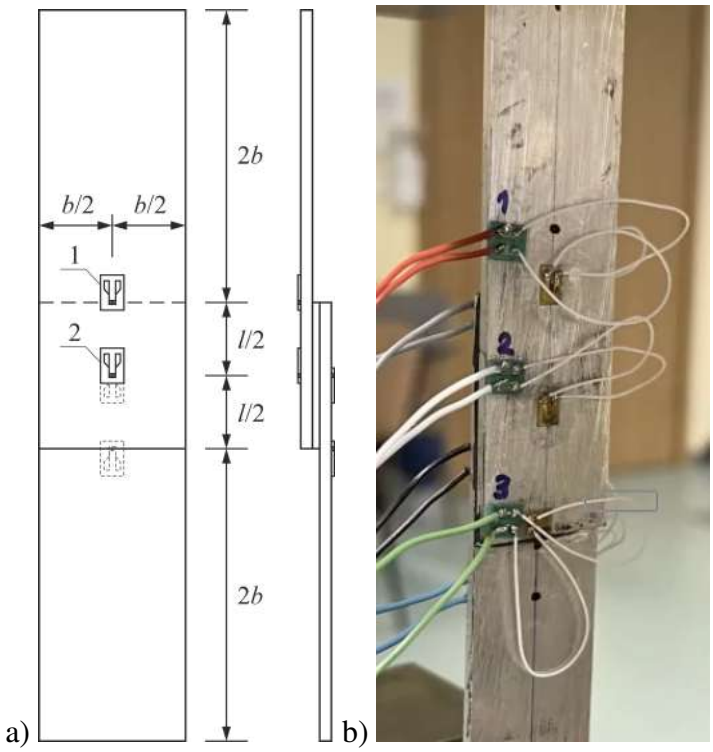

Figure 13: View of the test: a) diagram of the specimen with strain-gauge attachment points, b) specimen positioned in the grips of a universal testing machine

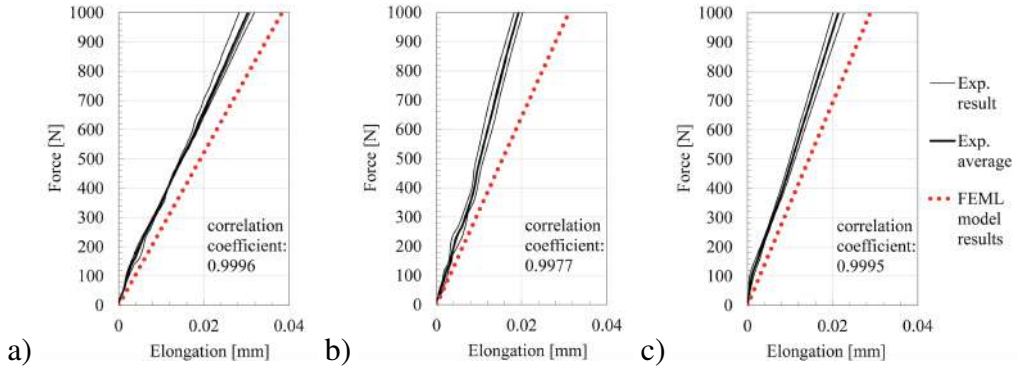

Figure 14: Experimental validation of the FEML model based on the load–elongation response of single-lap joints for overlap lengths a) $l = 12.5$ mm, b) 25 mm, and c) 37.5 mm, measured using a mechanical extensometer over a gauge length of $L_0 = 50$ mm, showing a comparison between experimental results and numerical predictions with corresponding correlation coefficients

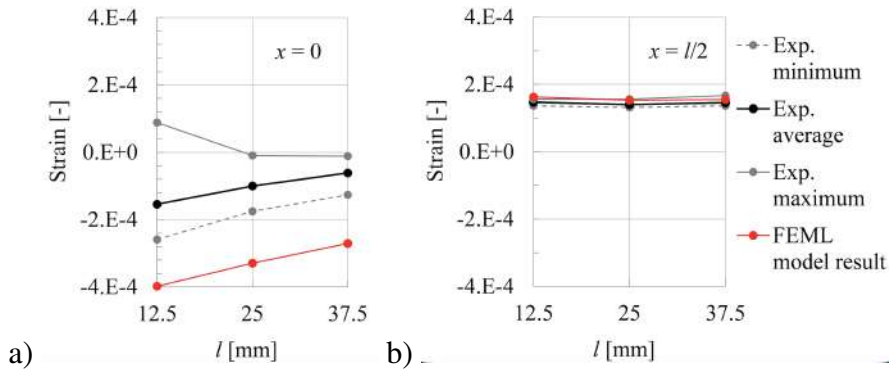

Figure 15: Comparison of experimentally measured and numerically predicted strains at selected locations within the overlap, namely a) at the beginning ($x = 0$) and b) at the mid-length ($x = l/2$), for overlap lengths $l = 12.5$, 25, and 37.5 mm

To obtain a dimensionless measure of the significance of interlayer slip, the following relative slip index was introduced

$$\delta_s = \frac{s_{\max}}{l} \cdot 100\%. \tag{74}$$

The parameter δ_s expresses the maximum interlayer slip relative to the joint length and therefore provides a direct measure of the degree of composite action. Values of δ_s close to 0% correspond to nearly full composite behavior (i.e., deformation close to that of a monolithic beam), whereas increasing δ_s indicates progressive interlayer decoupling and departure from the assumption of common cross-sectional action. For practical interpretation, the following ranges of δ_s may be adopted. When $\delta_s < 0.1\%$, the connection can be regarded as providing almost full composite action (Effectively monolithic). Slip is negligible in this range, and the structural response is very well represented by the solid (monolithic) beam model. For $0.1\% \leq \delta_s \leq 1\%$, a small but non-zero slip occurs (Partially composite). Nevertheless, the interaction between layers remains high, and the assumption of fully composite behavior is still justified as a reasonable engineering simplification. In the range $1\% < \delta_s \leq 5\%$, interlayer slip becomes noticeable. The solid beam model may still be applied, but it should be treated as an approximation, since partial interaction effects begin to influence the global structural response more significantly. When $\delta_s > 5\%$, the connection is considered weak and composite action is substantially reduced (Slip-dominated). In this case, analytical or numerical models that explicitly account for interlayer slip (e.g., shear-lag or partial interaction models) are required to accurately describe the mechanical behavior of

the system.

The analysis was carried out for three overlap lengths l=12.5, 25.0, and 37.5 mm (see Tab. 1). For each case, the FEM model provided the longitudinal displacement fields in both load-carrying layers, from which the slip distribution $s(x)$ and the maximum value $s_{\max}$ were obtained.

The obtained values of the relative slip index δ_s remain low for all analyzed overlap lengths (see Tab. 1). This indicates that the longitudinal displacement differences between the load-carrying layers are small compared to the characteristic length of the joint. Consequently, the layers deform in a highly coordinated manner, and the bonded structure exhibits behavior close to that of a monolithic beam.

At this point, it is also useful to clarify the interpretation of δ_s in relation to η. For large η, shear transfer through the adhesive layer is efficient, interfacial slip is strongly restrained, and δ_s remains small. In contrast, for low η, slip develops more extensively along the overlap, resulting in higher δ_s values and a reduced degree of composite action.

Furthermore, according to the criteria derived from equation (66), the constraints required to ensure a physically consistent representation of edge effects and adhesive thickness are generally satisfied for the geometric parameters adopted in the numerical example. In particular, the admissible range of the adhesive thickness t_3, resulting from the inequality given in (66), is fulfilled for all considered overlap lengths. For a constant adherend thickness $t = 1.9$ mm, this range can be expressed as follows: for $l = 12.5$ mm ($t/l = 0.152$), 0.004 mm $\leq t_3 \leq$ 0.05 mm; for $l = 25$ mm ($t/l = 0.076$), 0.015 mm $\leq t_3 \leq$ 0.05 mm; and for $l = 37.5$ mm ($t/l = 0.051$), 0.033 mm $\leq t_3 \leq$ 0.05 mm. However, it should be emphasized that the slenderness condition ($t/l \ll 1$), which constitutes an additional requirement of the model, is not satisfied for the shortest overlap length ($l = 12.5$ mm, $t/l = 0.152$). Finally, the value adopted in the analysis, $t_3 = 0.05$ mm, lies within the admissible range for all cases, although it is close to its upper bound. Therefore, the results should be interpreted with this limitation in mind.

All results of the numerical examples were compiled in Wolfram Mathematica, and a complete sample notebook (for l=b=25.0 mm) is included in the Digital appendix (https://drive.pg.edu.pl/s/bUwBtzGuG3BqnDk). The results of the numerical analysis are presented in Figs. 16–18, which show the distributions of normal, shear, and peel stresses in single-lap adhesively bonded joints with various overlap lengths: l=1/2b=12.5 mm, l=b=25.0 mm, and l=3/2b=37.5 mm. The results include a comparison of several analytical formulations – including the proposed solutions (Solutions I–III) and the classical theoretical models of Goland & Reissner and Hart-Smith - with FEM simulations and experimental data. It should be

Table 1: Maximum interlayer slip and relative slip index for different overlap lengths

l [mm]	$s_{\max}$ [mm]	δ_s [%]	Interpretation of composite action
12.5	0.0020	0.016	Effectively monolithic
25.0	0.0018	0.007	Effectively monolithic
37.5	0.0016	0.004	Effectively monolithic

noted that the original solution by Goland & Reissner was developed under the assumption of symmetric adhesive behavior with respect to the center of the overlap and using a coordinate system centered on the joint. However, in the equations presented in this paper (see (68), (69)) the coordinate system has been shifted to the beginning of the overlap region. Additionally, it should be noted that in the linear elastic beam model with displacement continuity adopted in this work, the adhesive layer corresponds, in the sense of the Goland & Reissner classification, to a relatively inflexible adhesive, for which the shear stress naturally vanishes at the overlap edges as a consequence of the assumed kinematics and equilibrium conditions. The three proposed analytical variants (Solutions I–III) differ in the physical effects they incorporate. Solution I neglects both bending and shear deformations in the adhesive layer, Solution II accounts for shear effects but omits bending, whereas Solution III includes both bending and shear deformations. Furthermore, as previously emphasized, Solution III represents the most general formulation, relying on only two primary assumptions: an elastic response of the joint and a thin adhesive layer.

Figure 16 shows the distribution of normal stresses along the joint for different overlap lengths. The results compare several analytical formulations and numerical data: Solution I (no bending/no shear deformations in the adhesive), Solution II (shear deformations included, bending neglected), Solution III (both bending and shear deformations included - shown at the top, middle, and bottom planes of the adhesive layer), the classical Goland & Reissner model, FEM predictions (with bending and shear deformations in the adhesive), and experimental measurements. For Solution III and the FEM model, the stress distributions are presented at three planes within the adhesive: the top, middle, and bottom. In contrast, Solutions I and II, as well as the Goland & Reissner formulation, describe the stresses only in the mid-plane of the upper adherend, which systematically underestimates the true stress levels, particularly near the joint entrance. It should also be noted that the Goland & Reissner solution describes only the average values of the normal stresses and their trends within the overlap, rather than their exact distribution.

Additionally, the experimental stresses in the direction of loading are shown for the upper adherend surface at the joint edge (x=0) and at the joint center (x=$l/2$). All approaches exhibit very similar global trends, with relatively small differences primarily associated with the overlap length (l=12.5, 25.0, and 37.5 mm). The largest discrepancies occur near the joint entrance (x=0, see Fig. 2). At the upper surface of the adherend, the normal stresses at x=0 are compressive and decrease from -31.3 MPa to -18 MPa (approximately 40%) as the overlap increases from 12.5 mm to 37.5 mm. The experimental results in this region agree with the predictions. Nevertheless, the discrepancies between Solution III or the FEM results and the experimental values arise from the sensitivity of the measurements to the exact positioning of the strain gauges. As noted earlier, the stresses decrease rapidly near the contact boundary – from the peak to almost zero within approximately 2 mm – and even with strain gauges of very small gauge length (0.6 mm), capturing the absolute peak values is practically impossible. Therefore, the experimental results shown in Fig. 16 represent average values at $x = 0$, rather than the true extremes. Furthermore, the slight overprediction of peak stresses by Solution III, relative to the FEM distributions, reflects the smoothing effects of numerical discretization. In contrast, the bottom fibres of the adherend experience tension, with stresses decreasing from 73.5 MPa to 60.3 MPa (approximately 20%) as the overlap length increases. The clear asymmetry between compressive stress at the upper fibres and tensile stress at the lower fibres results from bending in the adherends caused by the eccentricity of the load path, a feature captured only by Solution III and the FEM model. At the mid-plane of the adherend at x=0, no significant differences (less than 4%) are observed either between the analytical/numerical solutions (Solutions I–III, FEM) or with variations in overlap length. In this case, only the Goland & Reissner solution differs from the other solutions due to its inherent assumptions. The normal stresses at the midpoint of the joint at x=$l/2$ are always tensile and, regardless of overlap length (12.5, 25.0, or 37.5 mm), stabilize at approximately 10 MPa, i.e., about half of the average stress evaluated over the cross-section at x=0 (21.1 MPa). These mid-length values are further confirmed experimentally, and the agreement between experimental measurements and Solution III predictions is excellent. From a physical standpoint, the stresses within the bonded region reach stable, nearly uniform values once the load has been fully transferred between adherends. Interestingly, this stabilization distance is approximately 3.5 mm from the joint entrance, independent of overlap length, and thus may be interpreted as the characteristic load-transfer zone. Given the excellent agreement between Solution III and FEM predictions – both locally and globally – the proposed analytical formulation (Solution III) provides a

reliable and computationally efficient method suitable for preliminary design and assessment of bonded joints.

Figure 17 shows the shear stress distributions in the adhesive layer along the joint for different overlap lengths, as predicted by Solutions I, II, and III, and by the classical models of Goland & Reissner and Hart-Smith. The results are also compared with the FEM predictions. In general, the numerical results indicate that when bending in the joint is taken into account, unlike in approaches neglecting bending (Solutions I and II), increasing the overlap length reduces the extreme shear stresses in the adhesive and results in a more uniform stress distribution in the central region of the joint. Pronounced stress peaks remain at both ends of the joint, although their magnitudes decrease slightly as the overlap length increases, which is clearly visible in the FEM, Goland & Reissner and Solution III results. Solution III provides shear stress distributions that are rather consistent with FEM results and with the maximum values predicted by Hart-Smith's formulas. In contrast, the Goland & Reissner model, because of its linear formulation and neglect of adhesive thickness, significantly overestimates the peak stress values. For overlap lengths of 12.5, 25.0, and 37.5 mm, the FEM peak stresses are approximately -7.4 MPa, -6.8 MPa, and -6.4 MPa, respectively. The corresponding predictions by Goland & Reissner are approximately -23.6 MPa, -21.5 MPa, and -20.0 MPa, which represent an overestimation of approximately 70% relative to the FEM results. Solution III predicts approximately -7.9 MPa, -7.1 MPa, and -6.4 MPa, corresponding to an underestimation of about 1 percent relative to the FEM results. The Hart-Smith formulation predicts approximately -8.5 MPa, -8.2 MPa, and -8.1 MPa, corresponding to an underestimation of about 18 percent relative to the FEM results. This model is included in Fig. 17 in the form of the maximum shear stress $\tau_{3HS}^{\max}$, shown as a horizontal dashed line, and not as a shear stress distribution along the overlap length.

It should be emphasized that the shear stress maxima in the classical analytical solution of Goland & Reissner occur directly at the overlap edge, while in linear-elastic FEM analyses they appear almost directly at the edge. This behavior results from models idealizations, in particular the assumption of a perfectly sharp edge and linear elastic material behavior, and in the case of the Goland & Reissner solution additionally from the limiting assumption $t_3 \to 0$. In real adhesive joints such pointwise maxima do not occur because the stresses are distributed over a finite region near the edge. Therefore, the physically meaningful maximum stress should not be interpreted as the value at a single point, but rather as a maximum occurring within a small zone in the vicinity of the overlap edge.

In the proposed analytical solution (Solution III), the maximum shear stresses con-

sistently occur at a finite distance from the edge, equal to approximately 1 mm for the analyzed numerical cases. This distance is close to one half of the adherend thickness (about 1.9 mm) and remains independent of the overlap length. In the model it increases with the adherend thickness and approximately corresponds to one half of that thickness. This indicates that the shear stress distribution in the edge region is governed primarily by the bending stiffness of the adherends rather than by the very small but finite adhesive thickness (in the analyzed cases t_3=0.05 mm). As a result, the proposed solution (Solution III) provides physically realistic stress values representative of the actual edge region instead of the non-physical pointwise extrema occurring exactly at the edge in the classical Goland & Reissner formulation.

The proposed analytical model is formulated in terms of stresses averaged through the adhesive thickness and therefore represents a structural rather than local description of load transfer in the joint. Consequently, it does not reproduce the classical boundary-layer type stress singularity predicted by the Goland & Reissner solution or obtained in linear-elastic FEM models with an ideal sharp edge. Instead, the bending stiffness of the adherends introduces a characteristic transfer length of the order of the adherend thickness, which explains the finite position of the stress maximum and its weak dependence on the adhesive thickness.

This behavior should be understood as an intrinsic limitation of the adopted kinematic assumptions: the model captures effective stresses responsible for global force transfer but does not resolve local peak stresses associated with geometric or material singularities at the very edge of the overlap. Therefore, the solution is suitable for predicting overall load distribution and energetically relevant stress levels in the joint, but it should not be used for direct evaluation of crack initiation exactly at the edge or for phenomena governed by microscopic stress concentrations.

Figure 18 presents peel stress distributions in the adhesive layer for three overlap lengths, comparing Solution III with the classical models of Goland & Reissner and Hart-Smith, as well as FEM predictions. Solution III produces a slightly asymmetric distribution of peel stresses, which stems from the eccentric load transfer characteristic of single-lap joints. The induced bending leads to different local rotations of the adherends, so the peel stresses evaluated at the lower adhesive surface (at $z_1 = -t_1/2$, see Eqs. 49 and 52, where the adhesive thickness t_3 is explicitly included in subsequent derivation steps) are not perfectly symmetric, despite geometric and material symmetry. A similar asymmetry appears in the FEM model and symmetry is preserved only in the mid-plane of the adhesive, whereas local bending effects near the interfaces break it. The influence of joint length is

also evident. In Solution III, peak peel stresses decrease by approximately 12.5% with increasing overlap length. For the Hart-Smith model, this reduction is nearly 50%, for the Goland & Reissner formulation, it is nearly 28%, and for FEM, it is about 10%. Overall, Solution III - which accounts for both bending and shear deformations in the adhesive layer - matches FEM trends well and reproduces the qualitative behavior observed in the Hart-Smith model. It is worth emphasizing that, also in the case of peel stress analysis, Solution III provides the most realistic qualitative trends among all analysed approaches. Its ability to reproduce both the magnitude and spatial variability of peel stresses at different overlap lengths confirms its robustness and reliability. The inclusion of bending and shear deformations in the adhesive layer - while maintaining a fully closed-form formulation - makes Solution III a powerful analytical tool for the engineering assessment of bonded joints, enabling accurate predictions without the computational costs associated with FEM analysis.

Next, Fig. 19 presents the distributions of shear and peel stresses in the adhesive layer near the left overlap edge for $l = 25$ mm, highlighting the differences between analytical predictions and various FEM models in the region affected by edge singularities. In the case of shear stresses (Fig. 19a), significant discrepancies are observed in the immediate vicinity of the overlap edge, where both analytical and numerical solutions are strongly influenced by the singular stress field. The FEM results exhibit pronounced scatter and model-dependent variability in this region, confirming the lack of convergence associated with the singularity. Beyond the proposed exclusion zone ($\sim l_e$), however, the results obtained from different FEM models converge and show very good agreement with Solution III, which closely follows the reference values provided by the Hart-Smith model. It should be emphasized that the differences observed near the overlap edge arise from the fact that Solution III provides effective structural stresses, whereas the FEM results in this region reflect local singular stresses, which are not equivalent quantities. In contrast, the Goland & Reissner solution noticeably deviates, overestimating stress gradients and failing to capture the observed distribution. A similar trend is observed for peel stresses (Fig. 19b), although the region affected by strong gradients is more localized. The FEM results again reveal significant variability near the edge, while outside the exclusion zone a consistent and smooth stress distribution is obtained. Solution III provides an accurate representation of this behavior, capturing both the magnitude and the decay of peel stresses with high fidelity. The agreement between Solution III and FEM is particularly strong in the region governed by global load transfer, whereas discrepancies near the edge are attributable to the singular nature of the stress field rather than to deficiencies of

the model. Overall, the results confirm that a meaningful comparison between analytical and numerical solutions is only possible outside the singularity-dominated region. When interpreted in this manner, Solution III demonstrates very good predictive capability and provides a physically consistent description of both shear and peel stress distributions in the adhesive layer.

7. Conclusions

This paper examines the stress distribution in single-lap adhesive joints subjected to tensile loading. The analysis is based on theoretical formulations that account for variations in material properties, thickness, and joint length, under the assumption of a very thin adhesive layer. The proposed analytical solutions were validated using FEM simulations, experimental testing, and comparisons with established analytical models (Goland & Reissner and Hart-Smith).

The proposed analytical solutions inherently include limitations resulting from the assumptions of a very thin adhesive layer and linear-elastic material behavior. The stress analysis is performed using two-dimensional elasticity theory combined with the variational energy principle. Three analytical solutions (Solutions I, II, and III) are derived, each providing a different mechanical description of the same joint: initially, pure shear without deformation in the adhesive layer; subsequently, shear with adhesive deformation; and finally, a comprehensive formulation that also accounts for bending effects induced by eccentric tensile loading.

For the most general formulation (Solution III), an original expression was developed for the bending coefficients k, which depend on geometric and material parameters. This distinguishes the present approach from earlier analytical formulations. In addition, an original method was proposed to solve the governing system of differential equations for adhesive joints subjected to combined shear and bending. To the authors' knowledge, this approach has not previously been reported in the literature. Each solution is illustrated using numerical examples, with selected cases involving different overlap lengths. These represent only a subset of the potential applications of the general analytical formulation (Solution III). Importantly, Solution III is expressed in a general form, has a clear physical interpretation, and can be used for engineering design of single-lap adhesive joints – an area of growing relevance in practice.

However, it should be emphasized that in Solution III the adhesive layer is represented in an averaged, energetically equivalent sense, and the stress field across its thickness is not resolved explicitly. Consequently, the stresses predicted by this formulation should be interpreted as effective structural stresses rather than exact

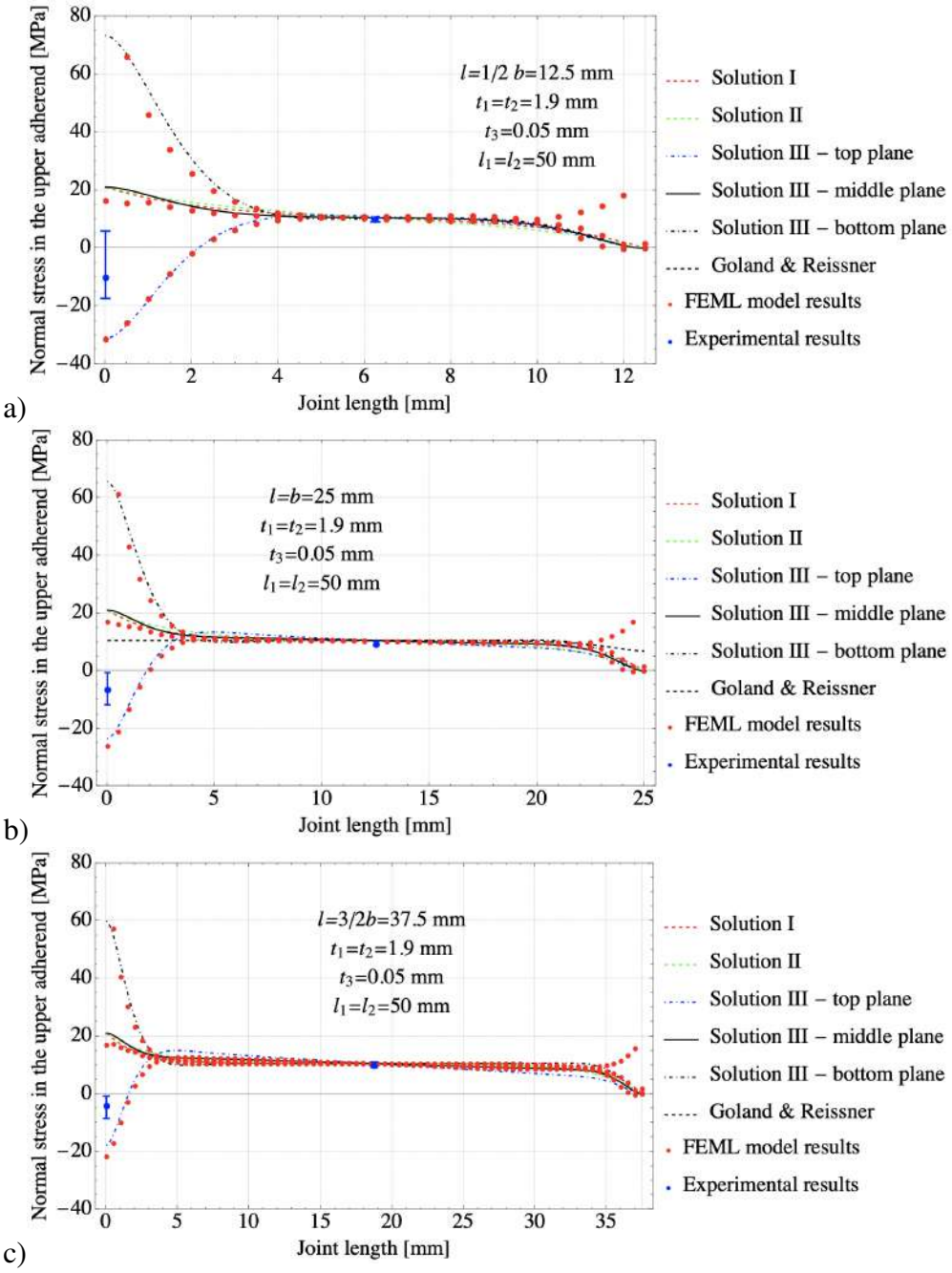

Figure 16: Normal stress in the upper part of the joint along the bond length for different overlap length parameters, evaluated in the FEML model at a distance of l_e=0.765 mm ($\sim 15t_3$) from the overlap edges to minimize edge singularity effects: a) $l=\frac{1}{2}b$=12.5 mm, b) $l=b$=25.0 mm, c) $l=\frac{3}{2}b$=37.5 mm

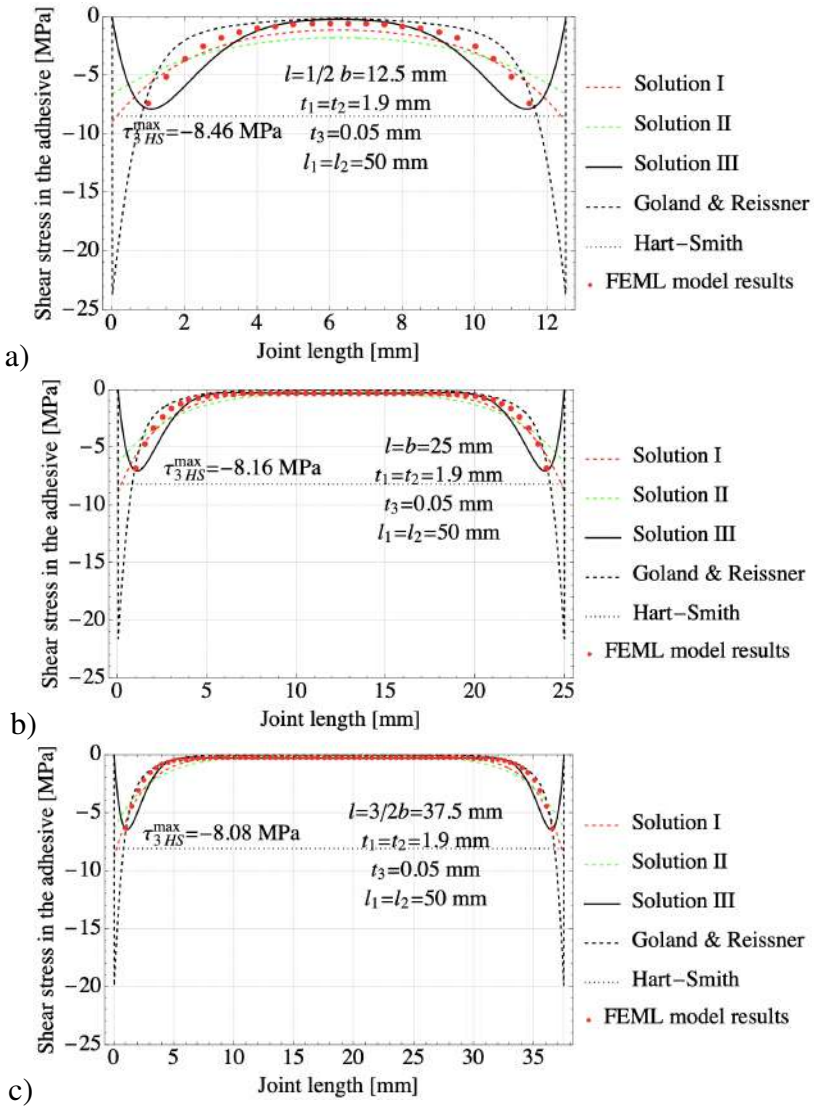

Figure 17: Shear stress in the adhesive along the length of the joint for different overlap length parameters, evaluated in the FEML model at a distance of l_e=0.765 mm (∼15t_3) from the overlap edges to avoid edge singularity effects: a) $l=\frac{1}{2}b$=12.5 mm, b) $l=b$=25.0 mm, c) $l=\frac{3}{2}b$=37.5 mm

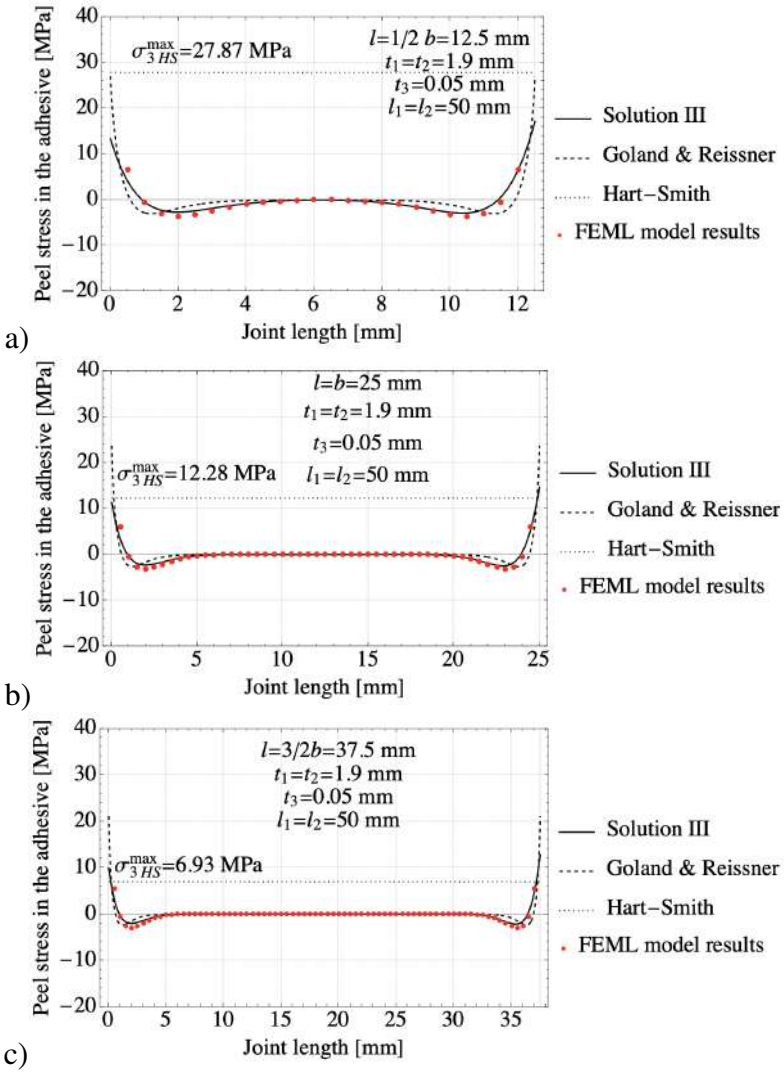

Figure 18: Peel stress in the adhesive along the length of the joint for different overlap length parameters, evaluated in the FEML model at a distance of l_e=0.765 mm ($\sim 20t_3$) from the overlap edges to reduce edge singularity effects: a) l=$\frac{1}{2}$$b$=12.5 mm, b) l=b=25.0 mm, c) l=$\frac{3}{2}$$b$=37.5 mm.

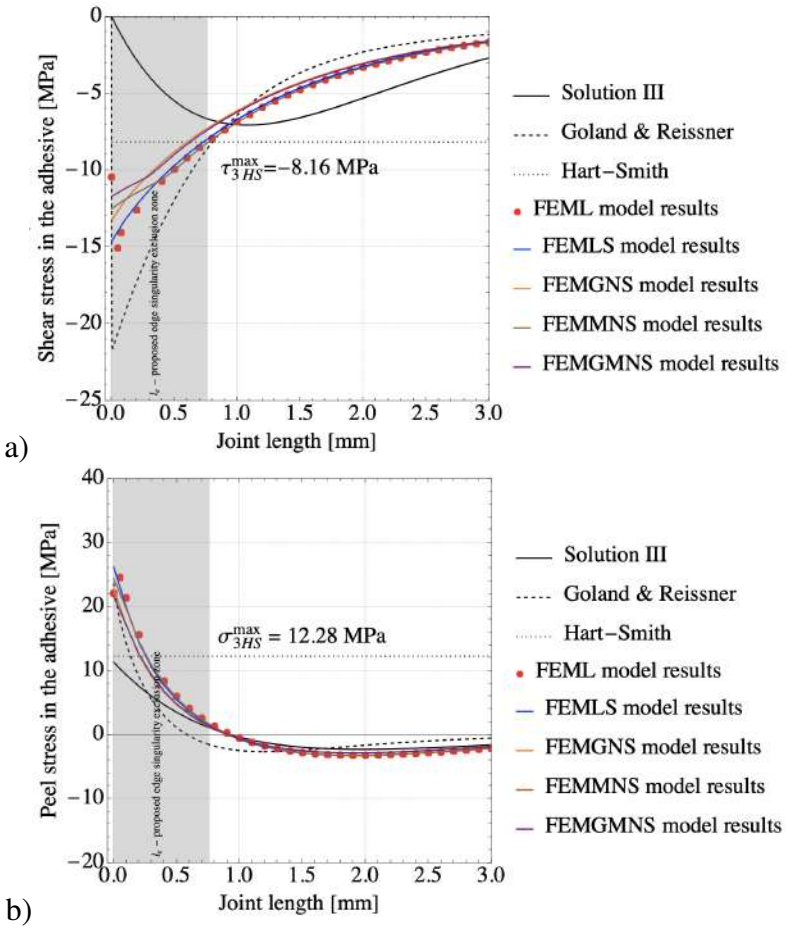

Figure 19: Distribution of shear and peel stresses in the mid-layer of the adhesive along the lap joint for $l = 25$ mm, shown for the left joint edge over the range 0-3 mm, based on results from analytical models and FEM, highlighting differences in the representation of the joint edge and including the proposed edge singularity exclusion zone: a) shear stress, b) peel stress

local adhesive stresses, particularly in the vicinity of the overlap edge where strong gradients and bi-material singular effects occur. For this reason, a finite reference distance from the overlap edge, denoted as l_e, is introduced in the present study, ensuring that the reported stresses are governed primarily by global load transfer rather than by local singular behavior.

A notable limitation of the present analysis also lies in the assumption of linear elastic behavior for both the adhesive layer and the adherends. While this simplification enables closed-form solutions and facilitates parametric investigations, it does not fully reflect the mechanical response of modern structural adhesives. Contemporary adhesive systems are frequently toughened through the incorporation of elastomeric or particulate phases, leading to pronounced nonlinear and elastic–plastic behavior accompanied by high fracture toughness. As a consequence, adhesively bonded joints are capable of sustaining significantly higher load levels, which may in turn induce nonlinear deformation not only within the adhesive layer but also in the adherends themselves. The relevance of such nonlinear effects has been recognized in the literature for several decades. Early nonlinear analysis were reported by Grimes et al. [52], followed by the plastic-zone modeling approaches introduced and subsequently extended by Fehrle et al. [53] and Goodwin [54]. More comprehensive contributions were later provided by Hart-Smith [55], who developed bi-linear elastic-plastic adhesive models and systematically investigated joint failure mechanisms associated with peel stresses, adhesive yielding, and adherend delamination. These studies demonstrate that linear elastic formulations may underestimate both the load-carrying capacity and the damage tolerance of adhesively bonded joints, particularly for ductile or toughened adhesive systems. Although the present study is intentionally restricted to elastic formulations, the implications of this assumption should be carefully considered when interpreting the results.

Linear and nonlinear FEM models were also developed to represent the behavior of the adhesive joint and to address numerical stress concentrations arising from singularities. These FE models provide a robust platform for validating the analytical predictions of Solution III and enable quantitative comparison with experimental measurements. Their configuration and application constitute original contributions that form a foundation for further studies of bonded joints with varying geometry and stiffness. In particular, two linear models were considered: the basic model without adhesive fillets (FEML) and the modified model including adhesive fillets (FEMLS). These models are compatible with the analytical formulation and provide a reliable basis for validating Solution III. A key issue in the FE analysis is the presence of both geometric and bi-material singularities at the overlap

edge, arising from the joint geometry and the strong mismatch in elastic properties between the adherends and the adhesive. This leads to mesh-dependent stress variations and prevents a physically meaningful interpretation of local stresses directly at the interface and near the joint edge. To overcome this limitation, stresses were evaluated at a finite distance from the edge, denoted as l_e, which defines an exclusion zone associated with the singular stress field. This approach ensures that the reported stresses reflect the global load transfer within the joint rather than local edge effects. In addition, nonlinear models incorporating geometric nonlinearity (FEMGNS), material nonlinearity (FEMMNS), and their combined effect (FEMGMNS) were developed to further assess the analytical solution in the nonlinear operating range of the joint, particularly near the overlap edge. Although nonlinear effects may partially reduce stress levels and mitigate the singularity, they do not eliminate the influence of the singular stress field entirely. Overall, the developed FEM models provide a physically consistent framework for validating the analytical predictions of Solution III and form a foundation for further studies of bonded joints with varying geometry, material properties, and nonlinear effects.
An important part of this work is the experimental testing, which - although fundamental in scope - provides basic validation of the analytical and numerical models. The results offer a reliable benchmark for assessing the accuracy of the analytical predictions and confirm their practical relevance. However, due to the complexity of the phenomenon and inherent measurement limitations, they do not resolve all underlying issues and should be regarded as complementary to the analytical and numerical analyses.
The numerical and experimental results demonstrate that the proposed analytical formulations, particularly Solution III, are capable of capturing the mechanical response of single-lap adhesive joints with high fidelity. It was observed that increasing the overlap length leads to a more uniform stress distribution and reduces peak shear and peel stresses, thereby improving overall load transfer. Furthermore, while the classical Goland & Reissner model significantly overestimates peak stress values, Hart-Smith's formulation and, most importantly, Solution III show good agreement with the FEM results, provided that regions affected by edge singularities are excluded, and the resulting stress distributions, when evaluated away from the immediate vicinity of the overlap edge, remain consistent with classical FEM and analytical results reported in the literature.
At the same time, it should be clearly stated - consistent with the assumptions of the model - that in Solution III the adhesive layer is represented in an averaged, energetically equivalent sense, and the stress field across its thickness is not resolved explicitly. Consequently, the stresses predicted by this formulation should be in-

terpreted as effective structural stresses rather than exact local adhesive stresses, particularly in the vicinity of the overlap edge, where geometric and bi-material singular effects dominate. Accordingly, the model provides a physically consistent description of global stress transfer but has limited capability in capturing local stress fields in the immediate vicinity of the interface.
Thus, the proposed models offer a reliable and physically transparent representation of stress distributions, balancing theoretical simplicity with predictive capability when interpreted within the framework of these assumptions and limitations.
In conclusion, the analytical solutions developed in this work - particularly Solution III - represent original contributions that complement existing research on adhesively bonded joints within the framework of classical analytical models. They extend these models through the introduction of a new expression for the bending coefficients k and provide a consistent linear framework capable of predicting effective stress distributions with satisfactory accuracy. An important aspect of this study is the integration of analytical, numerical, and experimental approaches, which is particularly valuable in the investigation of such complex phenomena. Overall, the proposed solutions provide a coherent basis for further refinement of analytical formulations and for their application in the design and optimization of structural adhesive joints.

Acknowledgements

Financial support from the National Science Centre, Poland, under grant no. 2023/07/X/ST8/00497, titled "Failure analysis in a single-lap adhesive joint of thin sheets," within the "MINIATURA 7" program is gratefully acknowledged.

This paper was also developed based on the statutory activities of the Poznan University of Technology (Grant from the Ministry of Science and Higher Education in Poland, no. 0612/SBAD/3640).

The calculations presented in the paper were carried out at the TASK Academic Computer Center in Gdańsk, Poland.

References

[1] O. Volkersen, The distribution of rivet forces in rivet connections subjected to tension with constant strap cross-sections, Luftfahrtforschung 15 (1938) 41–48 (in German).

[2] N. de Bruyne, The strenght of glued joints, Aircraft Engineering and Areospace Technology 16 (4) (1944) 115–118.

[3] M. Goland, E. Reissner, The stresses in cemented joints, Journal of Applied Mechanics 11 (1) (1944) A17–A27.

[4] L. Demarkles, Investigation of the use of rubber analog in the study of stress distribution in riveted cemented joints, Technical note 3413, National Advisory Committee for Areonautics (1955).

[5] A. McLaren, I. MacInnes, The infuence on the stress distribution in an adhesive lap joint of bending of the adhering sheets, British Journal of Applied Physics 9 (1958) 72–77.

[6] K. Hahn, D. Fouser, Methods for determining stress distribution in adherends and adhesives, Journal of Applied Polymer Science 6 (20) (1962) 145–149.

[7] E. Kuenzi, G. Stevens, Determination of mechanical properties of adhesives for use in the design of bonded joints, Tech. rep., U.S. Forest Service Research Note (1963).

[8] K. Masubuchi, R. Keith, Fundamentals of selected aspects of deformation characteristics of adhesive-bonded joints and metal-adhesive interfaces, Tech. rep., Battelle Memorial Institute (1967).

[9] L. Hart-Smith, Adhesive-bonded single-lap joints, Tech. rep., National Areonautics and Space Administration (1973).

[10] T. Wah, Stress distribution in a bonded anisotropic lap joint, Journal of Engineering Materials and Technology (1973).

[11] S. Yousefsania, M. Tahani, Analytical solutions for adhesively bonded composite single-lap joints under mechanical loadings using full layerwise theory, International Journal of Adhesion and Adhesives 43 (2013) 32–41.

[12] B. Zhao, Z.-H. Lu, Y.-N. Lu, Two-dimensional analytical solution of elastic stresses for balanced single-lap joints – variational method, International Journal of Adhesion and Adhesives 49 (2014) 115–126.

[13] R. Adams, E. Peppiatt, Effect of Poisson's ratio strains in adherends on stresses of an idealized lap joint, Journal of Strain Analysis 8 (2) (1973) 134–139.

[14] R. Adams, S. Chambers, P. del Strother, N. Peppiatt, Rubber model for adhesive lap joint, Journal of Strain Analysis 8 (1) (1973) 52–57.

[15] R. Adams, W. Wake, Structural adhesive joints in engineering, Elsevier, 1984.

[16] S. Cheng, D. Chen, Y. Shi, Analysis of adhesive-bonded joints with nonindentical adherends, Journal of Engineering Mechanics 117 (3) (1991) 605–623.

[17] D. Chen, S. Cheng, An analysis of adhesive-bonded single-lap joint, Journal of Applied Mechanics 50 (1983) 109–115.

[18] Z. Suo, J. Hutchinson, Interface crack between two elastic layers, International Journal of Fracture 43 (1990) 1–18.

[19] G. Fernlund, M. Papini, D. McCammond, J. K. Spelt, Fracture load predictions for adhesive joints, Composites Science and Technology (1994) 587–600.

[20] M. Papini, G. Fernlund, J. Spelt, The effect of geometry on the fracture of adhesive joints, International Journal of Adhesion and Adhesives 14 (1) (1994) 5–13.

[21] M. Tsai, J. Morton, An evaluation of analytical and numerical solutions to the single-lap joint, International Journal of Solids and Structures 31 (18) (1994) 2537–2563.

[22] L. Tong, Bond strength for adhesive-bonded single-lap joints, Acta Mechanica 117 (1996) 101–113.

[23] M. Tsai, D. Oplinger, J. Morton, Improved theoretical solution for adhesive lap joints, International Journal of Solids and Structures 35 (12) (1998) 1163–1185.

[24] S. Her, Stress analysis of adhesively-bonded lap joints, Composite Structures 47 (1999) 673–678.

[25] D. Romilly, R. Clark, Elastic analysis of hybrid bonded joints and bonded composite repairs, Composite Structures 82 (2008) 563–576.

[26] P. Schmidt, Modelling of adhesively bonded joints by an asymptotic method, International Journal of Engineering Science 46 (2008) 1291–1324.

[27] F. Ascione, Mechanical behaviour of frp adhesive joints: A theoretical model, Composites: Part B 40 (2009) 116–124.

[28] X. Wu, R. Jenson, Stress-function variational method for stress analysis of bonded joints under mechanical and thermal loads, International Journal of Engineering Science 49 (2011) 279–294.

[29] Z. Jiang, S. Wan, T. Keller, A. Vassilopoulos, Two-dimensional analytical stress distribution model for unbalanced frp composite single-lap joints, European Journal of Mechanics A/Solids 66 (2017) 341–355.

[30] M. Serpilli, R. Rizzoni, F. Lebon, Predictive asymptotic models of damage evolution in thin adhesives with tension–compression asymmetry, International Journal of Engineering Science 217 (2025) 104384.

[31] L. da Silva, P. das Neves, R. Adams, J. Spelt, Analytical models of adhesively bonded joints—part i: Literature survey, International Journal of Adhesion and Adhesives 29 (2009) 319–330.

[32] J. Wang, C. Zhang, Three-parameter, elastic foundation model for analysis of adhesively bonded joints, International Journal of Adhesion and Adhesives 29 (2008) 495–502.

[33] Y. Du, Y. Liu, F. Zhou, An improved four-parameter model on stress analysis of adhesive layer in plated beam, International Journal of Adhesion and Adhesives 91 (2019) 1–11.

[34] A. Crocombe, Modelling and predicting the effects of test speed on the strength of joints made with fm73 adhesive, International Journal of Adhesion and Adhesives 15 (1995) 21–27.

[35] L. Tong, A. Sheppard, D. Kelly, Relationship between surface displacement and adhesive peel stress in bonded double lap joints, International Journal of Adhesion and Adhesives 15 (1995) 43–48.

[36] X. Yu, A. Crocombe, G. Richardson, Material modelling for rate-dependent adhesives, International Journal of Adhesion and Adhesives 21 (2001) 197–210.

[37] M. A. W. Wahab, I. Ashcroft, A. Crocombe, P. Smith, Numerical prediction of fatigue crack propagation lifetime in adhesively bonded structures, International Journal of Fatigue 24 (2002) 705–709.

[38] M. Kujawa, A. Eremeyev, L. Smakosz, K. Winkelmann, P. Paczos, A. Piasecki, I. Kreja, Creep failure mechanism in single-lap joints, International Journal of Engineering Science 215 (2025) 104315.

[39] H. Chai, Shear fracture, International Journal of Fracture 37 (1988) 137–159.

[40] A. Crocombe, G. Richardson, Assessing stress state and mean load effects on the fatigue response of adhesively bonded joints, International Journal of Adhesion and Adhesives 19 (1999) 19–27.

[41] T. Keller, T. Vallée, Adhesively bonded lap joints from pultruded GFRP profiles. part I: stress–strain analysis and failure modes, Composites: Part B 36 (2005) 331–340.

[42] T. Sadowski, M. Kneć, P. Golewski, Experimental investigations and numerical modelling of steel adhesive joints reinforced by rivets, International Journal of Adhesion and Adhesives 30 (2010) 338–346.

[43] I. Lubowiecka, M. Rodríguez, E. Rodríguez, D. Martínez, Experimentation, material modelling and simulation of bonded joints with a flexible adhesive, International Journal of Adhesion and Adhesives 37 (2012) 56–64.

[44] A. Calabrese, A. Vassilopoulos, On the fatigue behavior of thin and thick adhesively bonded composite joints, International Journal of Fatigue 199 (2025) 109065.

[45] J. Reedy, Energy and variational methods in applied mechanics, John Wiley & Sons, Inc., 1984.

[46] I. Gelfand, S. Fomin, Calculus of variations, Dover Publications, 2000.

[47] A. Sazhin, Determining the stresses in glued joints between metal plates, Russian Engineering Journal 44 (1964) 45–49.

[48] I. Sneddon, Adhesives, The distribution of stress in adhesive joints, Oxford University Press, 1961, Ch. 9.

[49] M. Kujawa, P. Paczos, Ł. Smakosz, A. Piasecki, F. Jan, K. Winkelmann, V. Konopińska-Zmysłowska, V. A. Eremeyev, Impact of thermal and humidity conditions on structural epoxy adhesives during medium-term exposure, International Journal of Adhesion and Adhesives 139 (2025) 103981.

[50] W. Jiang, P. Qiao, An improved four-parameter model with consideration of poisson's effect on stress analysis of adhesive joints, Engineering Structures 88 (2015) 203–215.

[51] J. Bernaert, A. Calabrese, J. Botsis, A. Vassilopoulos, Automated crack propagation detection in adhesively bonded composite joints with digital image correlation techniques, Composites Part B 310 (2026) 113113.

[52] G. Grimes, L. Greimann, T. Wah, G. Commorford, W. Blackstone, G. Wolfe, The development of nonlinear analysis methods for bonded joints in advanced filamentary composite structures, Tech. rep., Southwest Research Institute (1972).

[53] A. Fehrle, J. Carroll, S. Freeman, Development of an understanding of the fatigue phenomena of bonded and bolted joints in advanced filamentary composite materials, Tech. rep., Lockheed-Georgia Co. (1972).

[54] F. Matthews, P. Kilty, E. Godwin, A review of the strength of joints in fibre-reinforced plastics. part 2. adhesively bonded joints, Composites 13 (1) (1982) 29–37.

[55] L. Hart-Smith, Designing to Minimize Peel Stresses in Adhesive-Bonded Joints, Vol. STP876-EB, ASTM International, 1985.

Appendix

$$
\begin{aligned}
a_1 &= \frac{2520Pt_1\left[3(k_1-1)t_1^2+3(k_1-2)t_1(t_2-2t_3)-4(t_2^2-3t_2t_3+3t_3^2)\right]}{b\overline{E}_2t_2},\\
a_2 &= -\frac{7560Pt_1(t_1+t_2-2t_3)\left[(k_1-1)t_1+(k_2-1)t_2+2t_3\right]}{b\overline{E}_2lt_2},\\
a_3 &= \frac{2520t_1\left[\overline{E}_2t_2^3+\overline{E}_1t_1\left(3t_1^2+6t_1t_2+4t_2^2-12(t_1+t_2)t_3+12t_3^2\right)\right]}{\overline{E}_1\overline{E}_2t_2},\\
a_4 &= \frac{1260t_1^3(t_1+t_2-2t_3)}{\overline{E}_2t_2},\\
a_5 &= -\frac{168t_1^2t_2}{\overline{E}_1\overline{E}_2\overline{E}_3}\Big\{5\overline{E}_2\overline{E}_3t_1t_2(2+3\overline{v}_1)+...\\
&+\overline{E}_1\overline{E}_3\left[9t_1^2+4t_2^2+36t_3^2+6t_2t_3(-1+5\overline{v}_2)+3t_1(t_2-12t_3-5t_2\overline{v}_2)\right]+...\\
&+30\overline{E}_1\overline{E}_2t_2t_3(1+\overline{v}_3)\Big\},\\
a_6 &= -\frac{42t_1^3t_2\left[5\overline{E}_2t_2(1+\overline{v}_1)+\overline{E}_1(6t_1+t_2-12t_3-5t_2\overline{v}_2)\right]}{\overline{E}_1\overline{E}_2},\\
a_7 &= \frac{6t_1^2t_2^2}{\overline{E}_1\overline{E}_2\overline{E}_3}\Big[21\overline{E}_2t_1^2(\overline{E}_3t_1+5\overline{E}_1t_3)+...\\
&+\overline{E}_1\overline{E}_3t_2\left(39t_1^2+22t_1t_2+4t_2^2-156t_1t_3-44t_2t_3+156t_3^2\right)\Big],\\
a_8 &= \frac{t_1^3t_2^2\left[\overline{E}_1\overline{E}_3t_2(39t_1+11t_2-78t_3)+7\overline{E}_2t_1(4\overline{E}_3t_1+15\overline{E}_1t_3)\right]}{\overline{E}_1\overline{E}_2\overline{E}_3},
\end{aligned}
\tag{75}
$$

$$
\begin{aligned}
a_9 &= \frac{2520Pt_1^2\left[(k_1-1)t_1 - t_2 + 2t_3\right]}{b\overline{E}_2 t_2},\\
a_{10} &= -\frac{2520Pt_1^2\left[(k_1-1)t_1 + (k_2-1)t_2 + 2t_3\right]}{b\overline{E}_2 l t_2},\\
a_{11} &= \frac{2520t_1^3\left(t_1 + t_2 - 2t_3\right)}{\overline{E}_2 t_2},\\
a_{12} &= \frac{420\left(\overline{E}_1 t_1^4 + \overline{E}_2 t_1 t_2^3\right)}{\overline{E}_1\overline{E}_2 t_2},\\
a_{13} &= -\frac{84t_1^3 t_2\left[5\overline{E}_2 t_2(1+\overline{v}_1) + \overline{E}_1(6t_1 + t_2 - 12t_3 - 5t_2\overline{v}_2)\right]}{\overline{E}_1\overline{E}_2},\\
a_{14} &= -\frac{84t_1^3 t_2\left(\overline{E}_1 t_1 + \overline{E}_2 t_2\right)}{\overline{E}_1\overline{E}_2},\\
a_{15} &= \frac{2t_1^3 t_2^2\left[\overline{E}_1\overline{E}_3 t_2(39t_1 + 11t_2 - 78t_3) + 7\overline{E}_2 t_1(4\overline{E}_3 t_1 + 15\overline{E}_1 t_3)\right]}{\overline{E}_1\overline{E}_2\overline{E}_3},\\
a_{16} &= \frac{t_1^4 t_2^2\left[13\overline{E}_3\left(\overline{E}_2 t_1 + \overline{E}_1 t_2\right) + 35\overline{E}_1\overline{E}_2 t_3\right]}{\overline{E}_1\overline{E}_2\overline{E}_3}.
\end{aligned}
\tag{76}
$$